

Benchmark Computation of Morphological Complexity in the Functionalized Cahn-Hilliard Gradient Flow

Andrew Christlieb^{1,2} Keith Promislow² Zengqiang Tan^{1,3}
 Sulin Wang^{2,*} Brian Wetton⁴ Steven Wise⁵

Abstract

Reductions of the self-consistent mean field theory model of amphiphilic molecule in solvent leads to a singular family of Functionalized Cahn-Hilliard (FCH) energies. We modify the energy, removing singularities to stabilize the computation of the gradient flows and develop a series of benchmark problems that emulate the “morphological complexity” observed in experiments. These benchmarks investigate the delicate balance between the rate of arrival of amphiphilic materials onto an interface and least energy mechanism to accommodate the arriving mass. The result is a trichotomy of responses in which two-dimensional interfaces grow by a regularized motion against curvature, pearling bifurcations, or curve-splitting directly into networks of interfaces. We evaluate second order predictor-corrector time stepping schemes for spectral spatial discretization. The schemes are based on backward differentiation that are either Fully Implicit, with Preconditioned Steepest Descent (PSD) solves for the nonlinear system, or linearly implicit with standard Implicit-Explicit (IMEX) or Scalar Auxiliary Variable (SAV) approaches to the nonlinearities. All schemes use fixed local truncation error to generate adaptive time-stepping. Each scheme requires proper preconditioning to achieve robust performance that can enhance efficiency by several orders of magnitude. The nonlinear PSD scheme achieves the smallest global discretization error at fixed local truncation error, however the IMEX scheme is the most computationally efficient as measured by the number of Fast Fourier Transform calls required to achieve a desired global error. The performance of the SAV scheme performance mirrors IMEX, at roughly half the computational efficiency.

Keywords: Phase Field Model; Benchmark Computations; Adaptive Time Stepping; Functionalized Cahn-Hilliard.

¹Department of Computational Mathematics, Science and Engineering, Michigan State University, East Lansing, MI 48824, USA

²Department of Mathematics, Michigan State University, East Lansing, MI 48824, USA

³School of Mathematics and Statistics, Huazhong University of Science and Technology, Wuhan 430074, China

*Corresponding author

⁴Department of Mathematics, University of British Columbia, Vancouver, BC V6T 1Z2, Canada

⁵Department of Mathematics, University of Tennessee, Knoxville, TN 37996, USA

E-mail addresses: christli@msu.edu (A. Christlieb), promislo@msu.edu (K. Promislow), tzengqiang@163.com (Z. Tan), wangsuli@msu.edu (S. Wang*), wetton@math.ubc.ca (B. Wetton), swise1@utk.edu (S. Wise)

1 Introduction

We present a series of physically motivated computational benchmark problems addressing the evolution of a gradient flow that develops rich morphological structures with slightly different energies whose faithful resolution requires significant computational accuracy. There has been considerable recent attention to the development of energy stable computational schemes for gradient descent flows [32, 33, 26, 27, 13, 14, 20, 34]. Gradient flows are defined by the dissipation of a free energy, and it is essential that numerical schemes preserve that property. Energy stable schemes have the desirable property that the energy, or a pseudo-energy, decreases at every time-step irrespective of time-step size. We argue that energy decay should be a consequence of accuracy, indeed energy decay without accuracy can mask poor performance by leading to plausible but incorrect computational outcomes. Accuracy should be balanced against computational cost, which motivates us to compare computational efficiency between schemes as measured by the minimal computational cost required to achieve a desired global discretization error.

Meaningful assessment of computational efficiency can be achieved from gradient flows that select from significantly different outcomes with subtle energy differences arising from strong nonlinear interactions. For motivation we emulate the “morphological complexity” experiments conducted by [22]. Dispersing amphiphilic diblock polymers in solvent and then allowing the mixture to relax, they observed the formation of a wide variety of structures whose evolution depended sensitively upon the polymer chain properties, see Figure 1 and [2, 1]. Reductions of the self-consistent mean field theory for a model of amphiphilic molecules in solvent leads to a singular family of Functionalized Cahn-Hilliard (FCH) energies, [6]. We modify these energies, mollifying the singularities to produce a family of computationally stable but highly nonlinear FCH gradient flows similar to those studied earlier, [17, 11, 12]. We present a series of benchmark problems that recover the onset of morphological complexity. These benchmarks reveal a delicate balance between the rate of arrival of amphiphilic materials onto an interface and the gradient flow’s selection of a least energy mechanism to redistribute them after absorption. This rate-based selection mechanism yields a trichotomy of responses in which two-dimensional interfaces either grow by a regularized motion against curvature, under-go pearling bifurcations, or directly curve-split into networks of interfaces. We present three numerical schemes, each combining second-order in time backward differentiation with a predictor-corrector approach and spectral spatial discretization. The FCH energy is computationally stiff. Each of the second order methods considered here balances implicit and explicit terms and their efficiency is very sensitive to the choice of the implicit terms, with improvements of several orders of magnitude possible when well pre-conditioned. These methods include an implicit-explicit (BDF2-IMEX) method and a scalar auxiliary variable approach (BDF2-SAV). The latter features provably unconditional pseudo-energy stability properties. Both of these schemes

are linear in their implicit stage. We compare these with a fully implicit, second order, backward differentiation scheme based upon a preconditioned steepest descent with approximate line search (BDF2-PSD) for the nonlinear solve. We will drop the 'BDF2' term in the sequel for brevity.

The FCH gradient flows possess many distinct, emergent timescales that preclude a fixed time-stepping approach. For each scheme a specified target local truncation error is used to generate an adaptive time-stepping procedure. The first set of benchmarks, the sub-critical, critical, and super-critical, use a relatively well conditioned form of the FCH energy, and vary the initial data to trigger bifurcations that lead to morphological complexity that engenders many possible outcomes in the super-critical case. A proper resolution of the time evolution requires considerable accuracy. The second set of benchmarks build significant stiffness into the FCH energy by increasing the second derivative of the well at the background state, mimicking the singular nature of the FCH energy. This adds a small foot to the left minima of the well, see Figure 2, hence these benchmarks are called Foot 1 and Foot 2. The stiffness increases the ratio of the absorption to the redistribution time-scales and also induces morphological complexity without change to initial data.

Each of the second order schemes we consider required a judicious choice of implicit terms or preconditioner. This choice was typically based upon the linearization of a residual about a spatially constant equilibrium solution. The linearly implicit IMEX and SAV accommodated the increase in stiffness for the Foot 1 and Foot 2 benchmarks without significant adjustment. The nonlinear solve in the PSD scheme required optimization of internal parameters, in particular an error tolerance associated to the iterative nonlinear solver, to converge. Moreover the efficiency of the PSD scheme decreased in comparison to the two linear implicit schemes with increasing numerical stiffness.

We conduct grid refinement studies to verify that each benchmark has an adequate spatial resolution and develop highly accurate solutions for each benchmark by an extensive computation with a very small local truncation error. Once spatially resolved, all three schemes yield concordant results for sufficiently small specified local truncation error. We adjust the local truncation error restriction and use short runs to tune performance parameters in each scheme for each benchmark, and record the accuracy and cost of each optimized scheme. At given local truncation error we find that the PSD approach is generically the most accurate and SAV is the least accurate, as measured by global error at the final time. However at fixed local truncation error the IMEX and SAV schemes required less computational effort than the PSD, with the IMEX scheme consistently requiring about half the computational effort of the SAV scheme. For these benchmarks a global L^2 discretization error of 3×10^{-2} was found to be a harbinger of accuracy, and within this constraint we viewed the local truncation error as an internal parameter to be adapted for each scheme to optimize global performance. For the sub-critical, critical, and super-critical benchmarks, all three schemes achieved this global accuracy with comparable efficiency although at quite different values of the local truncation error. As presented in Figure 15 achieving this accuracy for the super-critical

benchmark requires 1.5×10^5 , 2×10^5 , and 3×10^5 FFT calls for IMEX, PSD and SAV respectively. As the global error target was further tightened, the PSD scheme encountered increased computational effort, first increasing rapidly and then saturating. Conversely the computational effort of the IMEX and SAV schemes increases linearly with global discretization error related by a fixed factor of two. For the more strongly nonlinear benchmarks the efficiency of the linear-implicit schemes continued its linear relationship to global discretization error, and to each-other by the same factor of two. The efficiency of PSD deteriorated in comparison to the linear-implicit methods with increasing nonlinear strength, as depicted in Figure 16.

The SAV scheme is specifically designed to be energy stable with respect to an associated pseudo-energy. This property either assumes fixed time-stepping, which is impractical for the FCH gradient flows, or an adaptive time stepping based upon modifications by factors of two and nesting. This latter strategy was implemented for the super-critical benchmark and found to provide no benefit for accuracy while increasing computational cost by a factor of two to three. In all cases all convergent schemes preserved the energy decay property of the gradient flow.

In section 2 we sketch the derivation of a singular FCH model from a random phase approximation of self-consistent mean field theory, outline the regularization of the singular model to arrive at the family of FCH models studied here-in, and present the initial data and associated benchmark problems. This derivation is relevant as it illuminates the incorporation of the well-stiffness in the Foot 1 and Foot 2 benchmarks that is the initial motivation for this computational study. In section 3 we present the second-order adaptive numerical schemes which we use to resolve the benchmark problems and highlight the sensitivity of efficiency to choice of implicit terms. In section 4 we present an overview of the simulations of each of the five benchmark problems for a fixed local truncation error, showing where the schemes agree and disagree. In section 5 we contrast the performance of the schemes, particularly with respect to accuracy in the far-field of the domain, energy decay, evaluation of the precise critical value for onset of defects, and comparison of time-stepping performance and computational efficiency. We summarize the performance in section 6.

2 Mean field approximation of amphiphilic diblock suspensions

Self consistent mean-field (SCMF) approach derives density functional models that approximate the bulk interactions of collections of polymers represented by molecular units, [16]. When applied to amphiphilic diblock polymers suspended in a solvent the reduction yields a free energy for the three density components ϕ_i for $i = A, B, S$, which represents the hydrophilic head A and hydrophobic tail B of the diblock polymer and the solvent S , respectively. Considering a suspension of n_s solvent molecules and n_P polymer diblocks each comprised of N_A and N_B monomers of molecule A and B respectively, [8, 30] used the self-consistent mean field reduction to derive the free energy to a continuum phase-field model. More specifically, for $k = \{A, B, S\}$, they introduced the mean

densities

$$\bar{\phi}_A = \frac{n_P N_A}{|\Omega|}, \quad \bar{\phi}_B = \frac{n_P N_B}{|\Omega|}, \quad \bar{\phi}_S = \frac{n_S}{|\Omega|}, \quad (2.1)$$

and derived a bilinear approximation to the SCMF free energy expressed in terms of the variance from the mean $\phi_{k0} = \phi_k - \bar{\phi}_k$,

$$\mathcal{F}_{\text{UD}}^{(2)}(\phi_0) = \sum_{ij} \int_{\Omega} \frac{a_{ij}}{\sqrt{\bar{\phi}_i \bar{\phi}_j}} (D^{-1} \phi_{i0}) (D^{-1} \phi_{j0}) + \left(\frac{b_{ij}}{\sqrt{\bar{\phi}_i \bar{\phi}_j}} + \chi_{ij} \right) \phi_{i0} \phi_{j0} + \delta_{ij} \frac{c_{ij}}{\bar{\phi}_i} |\nabla \phi_{i0}|^2 dx. \quad (2.2)$$

Here $a = (a_{ij})$, $b = (b_{ij})$, $c = (c_{ij})$ denote material parameters and δ_{ij} is the usual Kronecker delta function. Their derivation is similar to [9], with both approaches incorporating long-range interaction terms through $D := (-\Delta)^{\frac{1}{2}}$, the square-root of the negative Laplacian subject to periodic boundary conditions. The long-range terms describe entropic effects of chain folding and volume exclusion derived from the interactions of the polymer chains with effective mean fields. A similar energy was proposed as a model of a microemulsions of oil, water, and surfactant by [29] who argued directly, and somewhat phenomenologically, from a Landau theory for a scalar density. This scalar model was extended to a more nonlinear one by [18] and [19], who proposed a density dependence on the coefficients. Uneyama and Doi also proposed a nonlinear extension, [31], for their vector model in which the average density $\bar{\phi}_k$ was replaced with the local density ϕ_k . This extrapolation yielded a family of models that include the Ohta-Kawasaki free energies. In [6] the nonlinear extrapolation approach was modified, first through a shift in dependent variables to the spatially averaged mean-zero density $\psi_k := D^{-1} \phi_{k,0}$, and then by an extrapolation step in which the average density $\bar{\phi}_k$ was replaced with a slowly varying average density,

$$\bar{\phi}_k \rightarrow \bar{\phi}_k (1 + \psi_k). \quad (2.3)$$

In addition, [6] reduced the three-component model to a scalar field similar to [19] by requiring a point-wise incompressibility, $\psi_A + \psi_B + \psi_S = 0$, and replacing the global constraint on the A- and B-polymer fractions with the point-wise constraint, $\phi_A/N_A = \phi_B/N_B$. This yields the parameterization

$$\psi_A = \psi_B = u/m_f, \psi_S = -u,$$

in terms of u that takes values in $(-m_f, 1)$. The resulting model depends upon $N_P := N_A + N_B$, the polymer fractions $\alpha_A = N_A/N_P$ and $\alpha_B = 1 - \alpha_A$, the polymer-solvent molecular mole fraction $m_f := n_P N_P / n_S$, and the dimensionless parameter $\varepsilon = \frac{l}{L} N_P^{1/2} \ll 1$ which rescales the Kuhn length l of the diblock polymer into a mean-square end-to-end length a single ideal diblock polymer chain expressed as a ratio of the domain length L . The amphiphilicity of the diblock molecules is expressed in terms of a weighted Flory-Huggins parameter

$$\chi_w := -\alpha_A \alpha_B \chi_{AB} + \alpha_A \chi_{AS} + \alpha_B \chi_{BS}, \quad (2.4)$$

where for $k, m \in \{A, B, S\}$ the Flory-Huggins parameters $\chi_{km} > 0$ record the strength of the repulsive interaction between a k -monomer and an s -monomer. The value of χ_w depends upon the composition of the polymer diblock chain, but not on its length. We assume strong hydrophobicity of the tail groups, which implies that $\chi_{BS} \gg \chi_{AB}$ and is reflected in the strong-hydrophobicity hypothesis

$$(\mathbf{H}^{\text{sh}}) \quad \chi_w > 0. \quad (2.5)$$

With these reductions and notation, [6] reduced the Uneyama-Doi bilinear energy (2.2) to the singular functionalized Cahn-Hilliard (S-FCH) form

$$\mathcal{F}_{\text{S-FCH}}(u) = \int_{\Omega} (\varepsilon^2 \Delta u - W'_S(u))^2 + P(u) dx, \quad (2.6)$$

where the singular potential W_S is given by

$$W'_S(u) = 24E(u) - 6m_f N_P (\ln |1 - u| + \chi_w u) + C_0. \quad (2.7)$$

For notational convenience we introduced the bulk exclusion term

$$E(u) = m_f \ln \left| 1 + \frac{u}{m_f} \right|, \quad (2.8)$$

which records the energy of small densities of polymer. Significantly E tends to $-\infty$ as u tends to $-m_f$ and is $O(m_f)$ elsewhere. The strong hydrophobicity assumption (\mathbf{H}^{sh}) guarantees that the potential W'_S has three zeros $b_l < b_M < b_r$ in the interval $(-m_f, 1)$. The well W_S is defined as the primitive of W'_S that has a double zero at $u = b_l$. Consequently W_S has two, generically unequal-depth, local minima at $u = b_l, b_r$ with $-m_f < b_l < 0 < b_r < 1$ for which $W_S(b_l) = 0 > W_S(b_r)$. The first derivatives of the well W_S are singular at the endpoints $u = -m_f$ and $u = 1$, corresponding to pure solvent and pure polymer phases. The perturbative potential P takes the form

$$P(u) := \frac{9}{\alpha_A \alpha_B} u^2 E'(u) - (W'_S(u))^2. \quad (2.9)$$

The constant C_0 does not impact the value of the energy for $u \in H^2_{\text{per}}(\Omega)$. It is chosen to minimize the the perturbative potential P .

2.1 Experimental motivation for the benchmark problems

We draw motivation for the benchmark simulations from the complexity observed in the experiments conducted in [22]. In that study the authors prepared well-stirred dispersions of amphiphilic diblock of Polyethylene oxide (PEO) - Polybutadiene (PB) in water, and allowed the mixture to relax and come to quasi-equilibrium. The weight fraction of polymer was fixed at 1%, and they considered a long and a short polymer chain, characterized by a fixed molecular length of the hydrophobic PB, with $N_{\text{PB}} (= N_B)$ taken as 45 and 170. They varied the aspect ratio $\alpha_A = N_A/N_B$,

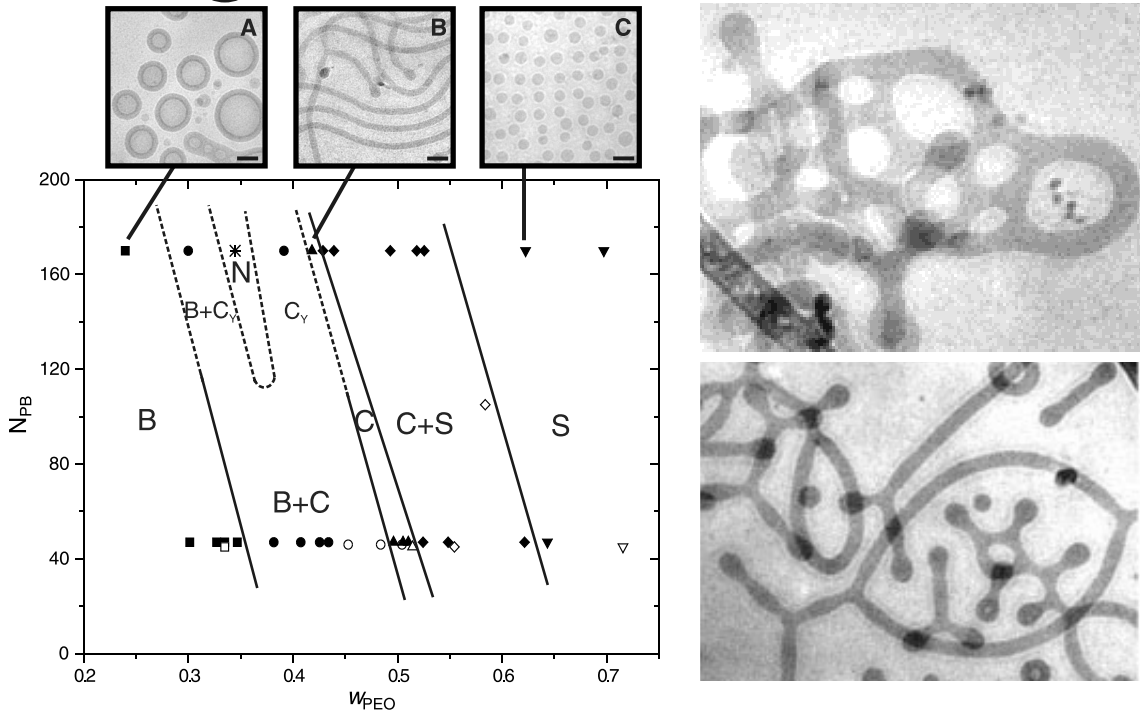


Figure 1: (left) Experimentally observed bifurcation diagram for the morphology of blends of Polyethylene oxide (PEO) - Polybutadiene (PB) amphiphilic diblock in water. The horizontal axis, w_{PEO} , is the weight fraction of PEO as a percent of the total diblock weight, and the vertical axis denotes the molecular weights of the PB component of the diblock, fixed at $N_{\text{PB}} = 45$ or 170 (vertical axis). *Morphological Complexity* is observed for $N_{\text{PB}} = 170$ but not for the shorter $N_{\text{PB}} = 45$ chains. (right) Experimental images from the morphological complexity regime showing (top) network structures and (bottom) a mixture of end caps and Y-junction morphology corresponding to regions marked N and C_Y in the bifurcation diagram. From Figures 1 and 2AC of [22], Reprinted with permission from AAAS.

characterized by the weight fraction, w_{PEO} , of the amphiphilic PEO component. They recovered a bifurcation diagram, presented in Figure 1 (left), which shows that for the short chains the well-mixed dispersions largely formed codimension one spherical bilayer interfaces, codimension two solid tubes, or codimension three solid spherical micelles, with some overlap depending upon the aspect ratio. However for $\alpha_A \in (0.3, 0.5)$ the suspensions of long chains form structures that are loaded with defects, such as the network structures and endcaps depicted in Figure 1 (right - top and bottom).

The self-assembly of spatially extended morphologies from a relatively dilute suspension can be viewed as an arrival and a redistribution process. The dispersed amphiphilic molecules are generically too dilute to self assemble, but may diffuse until they arrive at localized structure, insert themselves and lowering their contribution to the system energy by isolating their hydrophobic tail from contact with the solvent. Within the FCH model we study, the rate of arrival determines the final outcome of this growth phase. The selection mechanism for the end state is delicate, with

many possible outcomes separated by slightly different final energies. This landscape affords an excellent diagnostic to benchmark the performance of computational tools.

To regularize the benchmark problems we make several changes to the initial configuration and to the model. In particular we replace the well-stirred initial dispersion, typically modeled with random initial data, with a fixed bilayer interface configuration with an asymmetric shape and an added constant background of amphiphilic diblock that emulates the dispersed reservoir. The asymmetry in the shape seeds the motion against curvature, which in a benchmark problem is best not left to random fluctuations as would be the case for a perfectly circular initial shape. For computational reproducibility we smooth the well, replacing the singular W_S , especially its principle singularity at $u = -m_f$, with a smoother well W_q with parameter q that regulates its second derivative. As we shown in Figure 2, the most significant impact on the energy induced by the increase in the diblock polymer length is an increase in the value of W_S'' in the solvent phase. This raises the energy of a dilute, spatially constant suspension of the amphiphilic diblock molecule, as is consistent with the exposure of a long hydrophobic tail to solvent, [7].

Intuitively, both a high density of dispersed diblock polymers or a high energy associated to an isolated diblock molecule correspond to a high rate of absorption of the dispersed polymers onto the bilayer interface. This rate is a key quantity controlling defect formation. When the arrival rate is slow, the bilayer interface can grow in size to accommodate the new mass. The growth process is adiabatic and has been studied rigorously, [5], deriving a motion *against* curvature, regularized by a higher order Willmore term that includes surface diffusion. If the rate of arrival increases beyond a critical threshold, then defects, such as pearling, endcaps, and loop formation are observed. At moderate rates, a pearling bifurcation can be triggered, the onset of which is well understood within the context of the FCH gradient flow, [10]. The pearling can be transient, subsiding as the dilute suspension of amphiphilic material is consumed. The pearling can also lead to the formation of end-cap type defects, essentially micelles that remain connected to the underlying structure from which they emerged. The endcaps form most readily at points of high curvature of the bilayer interface. The stem of the endcap can grow, forming a long trailing bilayer-type stem and may ultimately reconnect with the initial structure, forming a loop. At yet higher arrival rates the bilayer interface itself may undergo curve splitting – directly forming closed loops and network structures. The rich array of possible outcomes, and the wide variety of end-states of the gradient flow, provide an excellent diagnostic of the accuracy of the proposed schemes.

Our benchmark problems stimulate the rate of arrival in two ways. In the first set of benchmarks we fix a smooth bilayer profile and a version of the non-singular well W_q with modest derivatives, determined by $q = 0$, and vary the initial background density of amphiphilic molecules. At a low background level, the sub-critical benchmark, the initial bilayer interface absorbs amphiphilic material and increases its length, however the rate is sufficiently slow that there is no generation

of defects. In the super-critical benchmark the background level is raised to induce the formation of several defects that coalesce and merge over time. In the critical benchmark the aspect ratio parameter η_2 is adjusted to trigger a more dramatic pearling transient within the bilayer interface. Accurate simulations in this benchmark approach but just fail to form an endcap before relaxing back to a smooth bilayer profile as the reservoir of dispersed diblock molecules is depleted. In the second set of benchmarks, we return to the initial data and systems parameters of the sub-critical case, but increase the value of $W_q''(b_-)$ by adjusting the value of q within the well. This increases the rate of absorption without adjusting the total amount of material absorbed, and induces defect formation.

2.2 FCH Model Calibration and Benchmarks

The FCH free energy with the non-singular well takes the form

$$\mathcal{E}_{\text{FCH}}(u) := \int_{\Omega} \frac{1}{2} \left(\varepsilon^2 \Delta u - W_q'(u) \right)^2 - \left(\frac{\varepsilon^2}{2} \eta_1 |\nabla u|^2 + \eta_2 W_q(u) \right) dx. \quad (2.10)$$

The FCH equation is given by the H^{-1} gradient flow of \mathcal{E}_{FCH}

$$u_t = \Delta \frac{\delta \mathcal{E}_{\text{FCH}}}{\delta u}, \quad (2.11)$$

which takes the explicit form

$$u_t = \Delta \left[(\varepsilon^2 \Delta - W_q''(u)) (\varepsilon^2 \Delta u - W_q'(u)) - (-\varepsilon^2 \eta_1 \Delta u + \eta_2 W_q'(u)) \right] \quad (2.12)$$

and the regularized double well potential is given by

$$W_q(u) := \left[\frac{(u - b_-)^2}{2} + q \varepsilon \left(1 - \text{sech}\left(\frac{u - b_-}{\varepsilon}\right) \right) \right] \left[\frac{(u - b_+)^2}{2} + \frac{\gamma}{3} \left(u - \frac{3b_+ - b_-}{2} \right) \right]. \quad (2.13)$$

We fix $b_{\pm} = \pm 1$ and take the asymmetry parameter $\gamma = 0.3$. The parameter q controls $W_q''(b_-)$, as depicted in Figure 2 (bottom), adding a small foot-like extension to the left-most local minima.

To compare the singular and the regularized wells it is convenient to exploit a rescaling of the FCH-SCMF energy that leaves the associated gradient flow invariant:

$$\varepsilon \rightarrow \frac{\varepsilon}{\sqrt{\nu}}, \quad W_S \rightarrow \frac{W_S}{\nu}, \quad P \rightarrow \frac{P}{\nu^2}, \quad t \rightarrow \nu^2 t.$$

The rescaling of ε is equivalent to a change in domain size $L \rightarrow \sqrt{\nu} L$. These rescalings simplify the process of adjusting the regularized well to fit the singular well under changes in the polymer chain length. We take each monomer to have equal weight, equal to the molecular weight of the solvent. Correspondingly the weight fraction of PEO, w_{PEO} , equals the molar fraction, α_A , and the polymer weight fraction within the solvent reduces to the molar fraction of polymer,

$$m_f = \frac{n_P N_P}{n_s} = \frac{1}{100}.$$

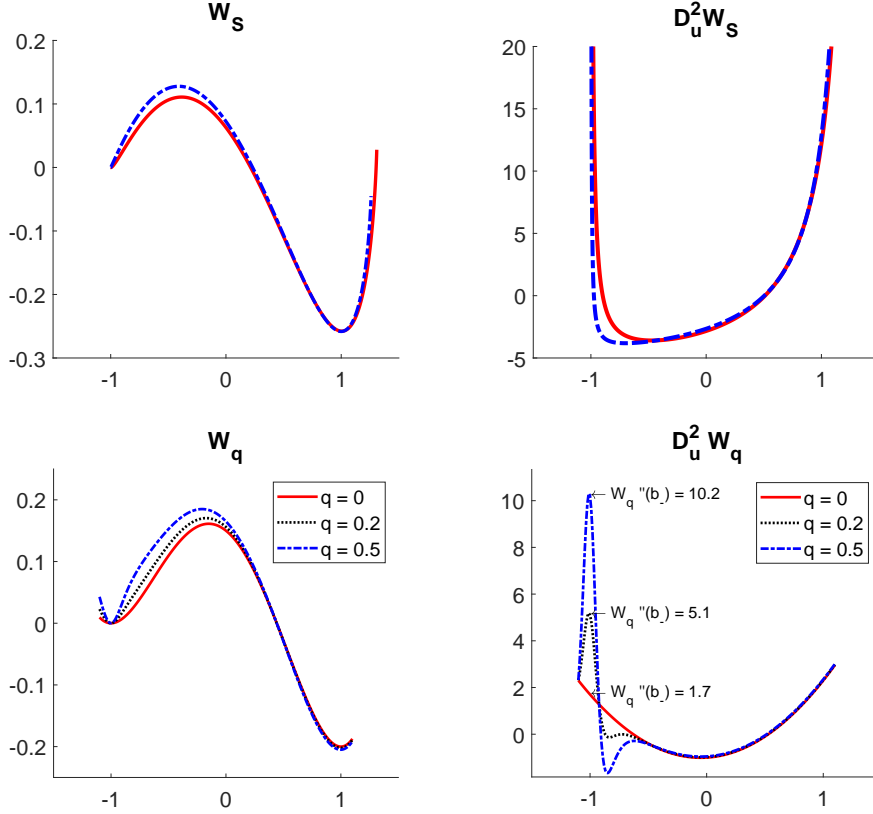


Figure 2: (top) Graph of scaled, translated singular well W_S and its second derivative as recovered by reduction of SCMF for $N_B = 45$ (red) and $N_B = 170$ (blue-dotted). (bottom) Graphs of the regularized well, W_q and its second derivative for $q = 0, 0.2, 0.5$.

For the benchmark problems that model the long and short chain polymers we take $\alpha_A = 0.3$, $m_f = 0.01$, and $\xi_w = 3$. For the short-chain polymer benchmark we take $N_P = 45$ and $C_0 = 0.8$ and for the long-polymer benchmark we take $N_P = 170$ and $C_0 = 3.0$, and rescale the well W_S by a factor of $\nu = 4.4$. For these parameters W_S has a first and singular second derivative at $u = -m_f = -0.01$ and the left well, defined by the left-most zero of W'_S , is located just to the right of this singularity, at $b_l = -0.0097$ for the short-chain polymers and at $b_l = -0.01 + 10^{-7}$ for the long-chain polymers. We rescale and translate

$$u \rightarrow 2 \frac{(u - b_l)}{b_r - b_l} - 1,$$

so that the left and right wells occur at $b_{\pm} = \pm 1$ as with W_q . The resulting W_S is presented in Figure 2 (top) and compared to the regularized well W_q used in the benchmark simulations. While Figure 2 (top-right) suggests that the second derivative of W_S is larger for the short chains, in fact the curves cross just to the right of $u = -1$, so that for the short chains $W_S''(-1) = 607$ while for the long chains $W_S''(-1) = 2022$, a ratio of 3.3.

The values of η_1 and η_2 for the sub-critical benchmark were determined from a least-square fit of P for the long-chain data to the form of the functionalization terms used in \mathcal{E} . For the other

benchmarks the values are reported in Table 1. For the critical case, the value of η_2 and d were tuned to enhance the strength of the pearling transient.

Table 1: Parameters for Benchmark Cases.

Case\Param	q	η_1	η_2	d	ε	γ	$\alpha_m(q)$	N	Mass
Sub-critical	0	1.45ε	3ε	0.2	0.1	0.3	1.7	256	6.11
Critical	0	1.45ε	1.5ε	0.75	0.1	0.3	1.7	256	7.61
Super-critical	0	1.45ε	3ε	0.5	0.1	0.3	1.7	256	6.93
Foot 1	0.2	1.45ε	3ε	0.2	0.1	0.3	5.1	256	6.11
Foot 2	0.5	1.45ε	3ε	0.2	0.1	0.3	10.2	512	6.11

2.3 The initial data

To construct the initial data, we fix $\Omega = [0, L]^2$ with $L = 4\pi$, $N = 256$ corresponding to a mesh spacing $\Delta x \approx 0.0491$. Given a simple non-intersecting parametric curve $\Gamma : \{(x(t), y(t)), t_0 \leq t \leq t_1\}$, we construct a region Γ_R of uniform width R about Γ , with outer and inner boundaries Γ_{\pm} defined by

$$\Gamma_{\pm} = \left\{ \left(x(t) \pm \frac{y'(t)}{s(t)}R, y(t) \mp \frac{x'(t)}{s(t)}R \right) \mid t_0 \leq t \leq t_1 \right\}, \quad (2.14)$$

where s is arc-length of Γ .

We construct the piece-wise constant function ϕ_{Γ} to be 1 inside Γ_R and -1 outside, and smooth it by convolution with the filter $\mathbb{F} : L^2(\Omega) \rightarrow C_{per}^{\infty}(\Omega)$ defined as

$$\mathbb{F}[\phi_{\Gamma}](x, y) = \sum_{k_1, k_2 \in I_N} \hat{\phi}_{\Gamma}(k_1, k_2) \exp(-\lambda_0(k_1^2 + k_2^2)) \exp\left(\frac{2\pi i}{L}(xk_1 + yk_2)\right),$$

where $\hat{\phi}_{\Gamma}$ is the discrete Fourier transform of ϕ_{Γ} interpolated to the $N \times N$ mesh with spacing $h = L/N$, and $\lambda_0 = 7.0269 \times 10^{-3}$. With the choice $R = 0.14725$ the total mass of $\mathbb{F}[\phi_{\Gamma}]$ per unit length of Γ approximates the mass of an exact bilayer dressing of Γ . For a fixed curve Γ we define $\phi_{256} := \mathbb{F}[\phi_{\Gamma}]$, which is fully spatially periodic. For higher resolution simulations, such as $N = 512$ or $N = 1024$ the corresponding ϕ_N is constructed by sampling ϕ_{256} on the finer grid.

For each of the benchmark cases we take the initial data in the form

$$u_0 = \phi_N + \varepsilon \frac{d}{\alpha_m^2(0)}, \quad (2.15)$$

where $d \in \mathbb{R}$ is a parameter that varies in the benchmarks and $\alpha_m(0) = W_q''(b_-)|_{q=0}$. The curve Γ is fixed, defined through polar variables as $\Gamma = \{(\rho(\theta) \cos(\theta) + \frac{L}{2}, \rho(\theta) \sin(\theta) + \frac{L}{2}) \mid \theta \in [0, 2\pi)\}$, where

$$\rho(\theta) = 3 - \frac{\varepsilon}{2} \cos\left(6\left(\theta - \frac{\pi}{11}\right)\right) - \varepsilon^2 \cos\left(\theta - \frac{3\pi}{11}\right).$$

The initial data u_0 corresponding to $N = 256$ with this choice of Γ is shown in Figure 3 (right) for $d = 0$. The curve Γ is chosen to break any symmetry with the periodic domain and to seed the curvature growth of the bilayer interface. The mass, m_0 , of the initial data, defined via the relation

$$m_0 := \frac{1}{2} \int_{\Omega} (u_0 + 1) dx,$$

is reported in Table 1.

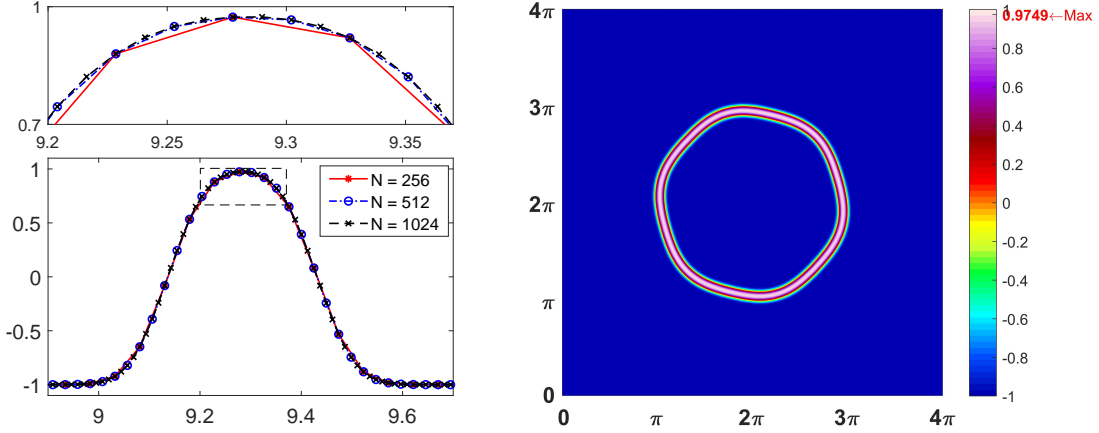


Figure 3: (left) A 1D cross-section of the profile ϕ_{256} and finer mesh realizations ϕ_{512} and ϕ_{1024} . (right) The initial data u_0 constructed from (2.15) with width $R = 0.14725$ and $d = 0$. The red number on the colorbar indicates $\max u$.

3 The Numerical Schemes

We use the 2nd order backward differentiation formula (BDF2) to produce the IMEX, PSD, and SAV schemes, and use the solution by the 3rd Adams-Moulton (AM3) scheme as a predictor to control the local error to resolve the benchmark problems described in Section 2.2.

3.1 Variable step size BDF2 and AM3 schemes

To solve the Cauchy problem: $y' = F(y)$, $y(t_0) = y_0$, and let us denote the temporal step size $k_n := t^n - t^{n-1}$, the classical uniform time-step BDF2 scheme is a 2nd order L-stable implicit linear multistep method

$$\frac{3y^{n+1} - 4y^n + y^{n-1}}{2k_n} = F(y^{n+1}).$$

We assume the variable step size BDF2 scheme has the form

$$ay^{n+1} + by^n + cy^{n-1} = F(y^{n+1}). \quad (3.1)$$

Taylor expanding both sides at $t = t^{n+1}$ and comparing the coefficients, we identify

$$\begin{cases} a = \frac{1}{k_{n+1}} + \frac{1}{k_{n+1} + k_n} \\ b = -\frac{1}{k_{n+1}} - \frac{1}{k_n} \\ c = \frac{1}{k_n} - \frac{1}{k_{n+1} + k_n} \end{cases}.$$

The classical uniform time-step AM3 scheme is a 3rd order (not A-stable) implicit linear multistep method reads

$$y^{n+1} = y^n + \frac{k_{n+1}}{6} \left[\frac{5}{2}F(y^{n+1}) + 4F(y^n) - \frac{1}{2}F(y^{n-1}) \right].$$

We assume the general variable step size AM3 scheme has the form

$$y^{n+1} = y^n + \left[\omega_1 F(y^{n+1}) + \omega_2 F(y^n) + \omega_3 F(y^{n-1}) \right].$$

To identify the coefficients $\{\omega_i\}_{i=1}^3$, we make the approximation

$$y(t^{n+1}) - y(t^n) = \int_{t^n}^{t^{n+1}} F(y(t)) dt \approx \int_{t^n}^{t^{n+1}} P(t) dt,$$

where the quadratic polynomial $P(t)$ is the interpolant of $F(y(t))$ at t^{n-1}, t^n and t^{n+1} . Introducing the time-step ratio $\tau := \frac{k_{n+1}}{k_n}$, the general variable step size AM3 scheme can be written as

$$y^{n+1} = y^n + \frac{k_{n+1}}{6} \left[\frac{3+2\tau}{1+\tau} F(y^{n+1}) + (3+\tau)F(y^n) - \frac{\tau^2}{1+\tau} F(y^{n-1}) \right]. \quad (3.2)$$

Further investigations can be found in [21].

3.2 Adaptive schemes

The FCH gradient flow undergoes bifurcations that trigger hidden timescales. As these events occur at unpredictable times, an adaptive approach to time-stepping is required to balance accuracy and efficiency. The FCH equation (2.11) has the form $u_t = F(u)$, where $F(u) = \Delta \frac{\delta \mathcal{E}_{\text{FCH}}}{\delta u}$. We set a local truncation error tolerance, σ_{tol} , and the minimal and maximal time-step values k_{\min} and k_{\max} .

Given $u^0 := u_0$, t^0 and some final time T , we fix the temporal step size $k_1 := k_{\min}$. Compute the first time-step u^1 , t^1 of the FCH equation (2.11) via the 1st order accurate scheme: the locally 2nd order BDF1-PSD, BDF1-IMEX and BDF1-SAV schemes for the PSD, IMEX and SAV schemes separately. For successive time steps we assume the index $n \in \mathbb{N}_+$, with u^{n-1}, u^n and a given temporal step-size k_n . The adaptive algorithm, based upon [28], initially sets $k = k_n$ and then proceeds as follows.

Step 1 Compute the 2nd order accurate main approximation \tilde{u}^{n+1} using a scheme with k_n, k .

Step 2 Compute the time step ratio $\tau = \frac{k}{k_n}$ and a 3rd order accurate approximation u_p through

$$u_p = u^n + \frac{k}{6} \left[\frac{3+2\tau}{1+\tau} F(\tilde{u}^{n+1}) + (3+\tau)F(u^n) - \frac{\tau^2}{1+\tau} F(u^{n-1}) \right], \quad (3.3)$$

Step 3 Calculate the relative error approximation $e_{n+1} := \frac{\|\tilde{u}^{n+1} - u_p\|_{L^2}}{\|u_p\|_{L^2}},$

Step 4 If $e_{n+1} \leq \sigma_{\text{tol}}$ or $k = k_{\min}$, then

save the solution $u^{n+1} = \tilde{u}^{n+1}$, the temporal step size $k_{n+1} = k$, the current time $t^{n+1} = t^n + k_{n+1}$,

and finally increase n by 1.

Recalculate the time step $k = \max\{k_{\min}, \min\{A_{dp}(e_{n+1}, k), k_{\max}\}\}$, where

$$A_{dp}(e, k) := \rho_s \left(\frac{\sigma_{\text{tol}}}{e} \right)^{1/3} k.$$

Goto **Step 1**.

We take the safety coefficient $\rho_s = 0.9$, and $k_{\min} = 10^{-9}$ for all simulations. For the IMEX and SAV schemes k_{\max} is taken to be ∞ , while for the PSD scheme, the optimal value of k_{\max} depends upon q , as shown in the Table 3. As discussed in [21], to ensure zero-stability for the variable step size BDF2 in (3.1), $A_{dp}(e, k)$ needs to be bounded from above by $(1 + \sqrt{2})k$. Numerical exploration with this bound on A_{dp} showed it afforded no significant impact on the benchmark problems.

3.3 The IMEX scheme

The FCH equation (2.12) can be rewritten as

$$u_t = \Delta \left[\mathcal{L}_{\text{IMEX}} u + \mathcal{N}_{\text{IMEX}}(u) + \varepsilon^2 \eta_1 \Delta u - \eta_2 W_q'(u) \right], \quad (3.4)$$

where we introduce the linear positive operator

$$\mathcal{L}_{\text{IMEX}} := \varepsilon^4 \Delta^2 - 2\alpha_m \varepsilon^2 \Delta + \alpha_m^2, \quad (3.5)$$

obtained by linearizing $\frac{\delta \mathcal{E}_{\text{FCH}}}{\delta u}$ in (2.12) about $u = b_-$ and dropping the small, negative η_1 and η_2 terms. Here $\alpha_m = W_q''(b_-)$ depends strongly on q . The term $\mathcal{N}_{\text{IMEX}}$ has zero linearization about $u = b_-$ and is given by

$$\mathcal{N}_{\text{IMEX}}(u) := \varepsilon^2 (\alpha_m - W_q''(u)) \Delta u + \varepsilon^2 \Delta (\alpha_m u - W_q'(u)) + W_q''(u) W_q'(u) - \alpha_m^2 u.$$

The resulting 2nd order semi-implicit IMEX scheme is chosen to stabilize the spatially constant background state $u \equiv b_-$. To this end we take the dominant linear terms implicit and the remainder, including smaller linear terms involving η_1 and η_2 , explicit,

$$au^{n+1} + bu^n + cu^{n-1} = \Delta \left[\mathcal{L}_{\text{IMEX}} u^{n+1} + \mathcal{N}_{\text{IMEX}}(u^{*,n+1}) + \varepsilon^2 \eta_1 \Delta u^{*,n+1} - \eta_2 W_q'(u^{*,n+1}) \right], \quad (3.6)$$

where

$$u^{*,n+1} := u^n + \frac{k_{n+1}}{k_n}(u^n - u^{n-1})$$

gives a locally second order extrapolated approximation at time level t^{n+1} to make sure the scheme is numerically consistent. Now we can isolate and solve u^{n+1} in (3.6) from

$$(a - \Delta \mathcal{L}_{\text{IMEX}})u^{n+1} = -bu^n - cu^{n-1} + \Delta \left[\mathcal{N}_{\text{IMEX}}(u^{*,n+1}) + \varepsilon^2 \eta_1 \Delta u^{*,n+1} - \eta_2 W'_q(u^{*,n+1}) \right]. \quad (3.7)$$

3.4 The PSD scheme

To PSD attempts to solve (2.12) via a general implicit set up

$$au^{n+1} + bu^n + cu^{n-1} = \Delta \left. \frac{\delta \mathcal{E}_{\text{FCH}}}{\delta u} \right|^{n+1}. \quad (3.8)$$

Given u^{n-1} and u^n , the equation for u^{n+1} is defined in terms of the zero of the negative of the residual,

$$\mathcal{R}(u^{n+1}; u^n, u^{n-1}) := \Pi_0 \left. \frac{\delta \mathcal{E}_{\text{FCH}}}{\delta u} \right|^{n+1} - \Delta^{-1}(au^{n+1}) - \Delta^{-1}(bu^n + cu^{n-1}) = 0, \quad (3.9)$$

where Π_0 denotes the linear zero-mass orthogonal projection operator. The preconditioned steepest descent (PSD) method solves this nonlinear system (3.9) iteratively through a series of linear systems. We introduce \mathcal{L}_{PSD} , the linearization of (3.9) about the spatially constant state $u^{n+1} \equiv b_-$ and dropping the small η_1 and η_2 terms,

$$\mathcal{L}_{\text{PSD}} := \varepsilon^4 \Delta^2 - 2\alpha_m \varepsilon^2 \Delta + \alpha_m^2 - a\Delta^{-1}.$$

This strictly positive, self-adjoint operator is well-defined on mass-less functions, and preconditions the iterative scheme. The search direction d_s^{n+1} at u_s^{n+1} is defined as

$$d_s^{n+1} := -\mathcal{L}_{\text{PSD}}^{-1} \mathcal{R}(u_s^{n+1}, u^n, u^{n-1}).$$

The solution u^{n+1} is defined as the limit of the sequence $\{u_s^{n+1}\}_{s=0}^\infty$, constructed through the approximate line search (ALS) recurrence relation

$$u_0^{n+1} := u^n + \frac{k_{n+1}}{k_n}(u^n - u^{n-1}), \quad (3.10)$$

$$u_{s+1}^{n+1} = u_s^{n+1} + \lambda d_s^{n+1}, \quad s = 0, 1, 2, \dots \quad (3.11)$$

This solver is referred to as the PSD with approximate line search (ALS) algorithm, see [15, 3]. For a prescribed iterative stopping tolerance i_{tol} , the ALS scheme is terminated once $\frac{\|d_s^{n+1}\|_{L^2}}{\|u_{s+1}^{n+1}\|_{L^2}} < i_{\text{tol}}$. The parameter λ in (3.11) is the search-step-size. Numerical investigations show that the optimal value of λ is somewhat sensitive to the value of $\alpha_m = \alpha_m(q)$ and k . This dependence was determined by minimizing the average number of PSD iterations for a fixed k over the first 50 temporal steps

Table 2: Dependence of optimal value of search-step-size λ on temporal step size k .

k	$\leq 10^{-6}$	$5 \cdot 10^{-6}$	10^{-5}	$5 \cdot 10^{-5}$	10^{-4}	$5 \cdot 10^{-4}$	10^{-3}	$5 \cdot 10^{-3}$	0.01	0.02	0.03
$q = 0$	1	1.05	1.07	1.11	1.14	1.24	1.34	1.60	1.738	1.804	1.855
$q = 0.2$	1	1.01	1.04	1.15	1.28	1.50	1.70	1.87	1.92	1.95	1.97
$q = 0.5$	1	1.16	1.20	1.32	1.45	1.72	1.83	1.965	1.97	1.985	1.99

of the simulation. Optimal values of λ for different values of q and k are reported in Table 2. The values used in the simulations were determined by linear interpolation.

The iterative stopping tolerance, i_{tol} , impacts the accuracy and computational cost of the PSD scheme. Numerical optimization finds that an optimal choice of i_{tol} is sensitive to both the well stiffness, q and the local truncation error, σ_{tol} . We determine this relation through the ratio

$$i_{\text{tol}} = \nu(q)\sigma_{\text{tol}},$$

and determine an optimal value of $\nu(q)$. This requires balance, as overly small values of i_{tol} lead to excessive iterations that do not improve the scheme's accuracy. On the other hand i_{tol} must be small enough to ensure that numerical error from the iterative solver does not pollute the adaptive time-stepping and does not impede the convergence of the iterative solver at subsequent time-steps. Instructively, the iterative convergence rate was found to depend upon the upper limit, k_{max} , imposed on the adaptive time-stepping algorithm. This lead to a coupled numerical optimization study, presented in Table 3 which shows the sensitivity of iterations numbers upon k_{max} for the three values of q , and the optimal value of ν . The iteration counts increase considerably with q , while ν decreases exponentially with q . If the upper bound k_{max} is removed then the iteration count may increase considerably, with associated increase in computational effort. The tuning of k_{max} and ν with q was the most unpredictable element of the optimization process for any of the three schemes.

Table 3: Dependence of PSD iteration count on ν and k_{max} .

Iteration count/1000	$\nu(q)$	Value of k_{max}							optimal k_{max}
		0.009	0.01	0.02	0.03	0.04	0.05	0.06	
$q = 0$	1.E-03		36.3	34.8	36.5	36.7	38.2	41.4	0.05
$q = 0.2$	2.E-05		43.3	42.8	43.7				0.02
$q = 0.5$	1.E-06	162.0	161.7	162.0					0.01

3.5 The SAV scheme

Computational schemes based upon the SAV formulation have been applied to the FCH gradient flow, see [34]. The version presented here is a slight variation. We rewrite the FCH energy functional $\mathcal{E}_{\text{FCH}}(u)$ in (2.10) in the form:

$$\mathcal{E}_{\text{FCH}}(u) = \int_{\Omega} \left[\frac{\varepsilon^4}{2} (\Delta u)^2 - \left(\frac{\eta_1}{2} + \zeta \right) \varepsilon^2 |\nabla u|^2 + G(u) \right] dx, \quad (3.12)$$

where $\zeta > 0$ is a parameter and

$$G(u) := -\varepsilon^2 \Delta u (W'_q(u) + \zeta u) + \frac{1}{2} (W'_q(u))^2 - \eta_2 W_q(u). \quad (3.13)$$

The choice of principle linear operator for the SAV scheme is a bit less intuitive than for the IMEX or PSD schemes. We introduce

$$\mathcal{L}_{\text{SAV}} = \varepsilon^4 \Delta^2 + \varepsilon^2 (\eta_1 + 2\zeta) \Delta = \mathcal{L}_0 + \mathcal{L}_1, \quad (3.14)$$

where the sub-operators are parameter dependent

$$\mathcal{L}_0(\beta_1, \beta_2) = \varepsilon^4 \Delta^2 - \beta_1 \alpha_m \varepsilon^2 \Delta + \beta_2 \alpha_m^2, \quad (3.15)$$

$$\mathcal{L}_1(\beta_1, \beta_2) = \varepsilon^2 (\eta_1 + 2\zeta) \Delta + \beta_1 \alpha_m \varepsilon^2 \Delta - \beta_2 \alpha_m^2, \quad (3.16)$$

where $\alpha_m = \alpha_m(q)$ and the constants $\beta_1, \beta_2 \geq 0$ are the stabilization parameters. The operator \mathcal{L}_0 defines the principle linear implicit terms in the SAV scheme. The default choice for these parameters is $\beta_1 = 0$ and $\beta_2 = 3$.

Introducing the auxiliary energy

$$\mathcal{E}_1(u) = \int_{\Omega} G(u) dx,$$

the FCH energy (3.12) takes the form

$$\mathcal{E}_{\text{FCH}}(u) = \frac{1}{2} (u, \mathcal{L}_{\text{SAV}} u)_{L^2(\Omega)} + \mathcal{E}_1(u). \quad (3.17)$$

For fixed time-steps the SAV scheme is known to be pseudo-energy stable for an auxiliary energy, if the functional $\mathcal{E}_1(u)$ can be shown to be uniformly bounded from below over $H_{\text{per}}^2(\Omega)$, [26]. This is achieved by choice of $\zeta = \zeta(q)$. Specifically

$$\mathcal{E}_1(u) \geq \int_{\Omega} \left(W''_q(u) + \zeta \right) |\nabla u|^2 dx + \int_{\Omega} \left[\frac{1}{2} (W'_q(u))^2 - \eta_2 W_q(u) \right] dx,$$

and choosing ζ larger than negative of the minimum of W''_q , see Figure 2, then the first integral is positive and we estimate

$$\mathcal{E}_1(u) \geq |\Omega| \min_u \left(\frac{1}{2} (W'_q(u))^2 - \eta_2 W_q(u) \right) > -D_0,$$

where $D_0 > 0$ only depends upon the domain Ω , the value of η_2 and the form of W_q .

For the energy splitting approach, we introduce the scalar auxiliary variable

$$r = r(t) := \sqrt{\mathcal{E}_1(u) + D_0},$$

then the FCH equation can be rewritten as

$$\frac{\partial u}{\partial t} = \Delta \mu, \quad \mu := \mathcal{L}_{\text{SAV}} u + \frac{r}{\sqrt{\mathcal{E}_1(u) + D_0}} V[u], \quad (3.18)$$

$$\frac{dr}{dt} = \frac{1}{2\sqrt{\mathcal{E}_1(u) + D_0}} \int_{\Omega} V[u] \frac{\partial u}{\partial t} dx, \quad (3.19)$$

where $V[u] = \delta \mathcal{E}_1 / \delta u = G'(u)$. The SAV scheme takes the form

$$au^{n+1} + bu^n + cu^{n-1} = \Delta \mu^{n+1}, \quad \mu^{n+1} = \mathcal{L}_0 u^{n+1} + \mathcal{L}_1 u^{*,n+1} + \frac{r^{n+1}}{\sqrt{\mathcal{E}_1(u^{*,n+1}) + D_0}} V[u^{*,n+1}], \quad (3.20)$$

$$ar^{n+1} + br^n + cr^{n-1} = \int_{\Omega} \frac{V[u^{*,n+1}]}{2\sqrt{\mathcal{E}_1(u^{*,n+1}) + D_0}} (au^{n+1} + bu^n + cu^{n-1}) dx, \quad (3.21)$$

where $u^{*,n+1}$ can be chosen as any explicit approximation of $u(t^{n+1})$ with an error of $\mathcal{O}(k^2)$, for instance,

$$u^{*,n+1} = u^n + \frac{k_{n+1}}{k_n} (u^n - u^{n-1}).$$

We remark that the r^{n+1} variable in (3.21) also contribute to the implicit equation for u^{n+1} . The full resolution of u^{n+1} from (3.20)–(3.21) is presented in [34, 28], but is driven by the inversion of the operator $\mathcal{L}_0 - a\Delta^{-1}$. With a fixed time-step k , the SAV scheme is unconditionally energy stable for the auxiliary energy

$$\mathcal{E}_{\text{aux}}(u_{n+1}, u_n, r_n, r_{n-1}) := \mathcal{E}_{\text{FCH}}(u_{n+1}) + \left(u_{n+1} - \frac{u_n}{2}, \mathcal{L}_{\text{SAV}} \left(u_{n+1} - \frac{u_n}{2} \right) \right)_{L^2(\Omega)} + (2r_n - r_{n-1})^2.$$

That is, for any choice of time-step $k > 0$, the auxiliary energy has the property

$$\mathcal{E}_{\text{aux}}(u_{n+2}, u_{n+1}, r_{n+1}, r_n) \leq \mathcal{E}_{\text{aux}}(u_{n+1}, u_n, r_n, r_{n-1}), \quad n \geq 1.$$

See [28] for details on the energy stability properties of SAV schemes.

The stabilization parameters makes \mathcal{L}_0 a strictly positive operator and play an essential role in the convergence, accuracy, and efficiency of the SAV scheme. The operator \mathcal{L}_0 reduces to $\mathcal{L}_{\text{IMEX}}$ for the choice $\beta_1 = 2$ and $\beta_2 = 1$. Figure 4 shows FFT counts for simulations of IMEX and SAV using the dominant implicit term based on \mathcal{L}_0 . Overall the schemes perform well if $\beta_1 + \beta_2 = 3$, with performance deteriorating dramatically for smaller values and slowly for larger values of this sum. Indeed values of $\beta_1 + \beta_2 < 3$ can lead to FFT counts that are several orders of magnitude higher per time-unit at fixed local truncation error. The left panel provides total FFT counts for the IMEX scheme with $\beta_2 = 3 - \beta_1$, showing that the performance is optimal so long as neither β_1 nor β_2

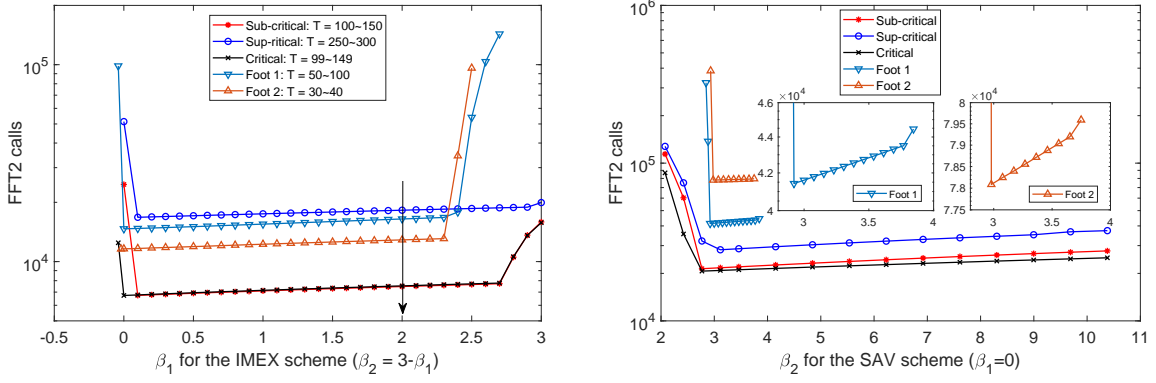


Figure 4: Total FFT calls versus stabilization parameters β_1 and β_2 for IMEX and SAV for each of the 5 benchmark simulations. (left) Total FFT calls versus β_1 for IMEX with $\beta_2 = 3 - \beta_1$. The choice $\beta_1 = 2$ used in IMEX simulations herein is indicated with black arrow. (right) Total FFT calls as function of β_2 for $\beta_1 = 0$ for the SAV scheme.

are too small. The choice $\beta_1 = 2$ is the default for IMEX. The right panel shows performance of the SAV scheme with $\beta_1 = 0$ for a range of value of β_2 for each of the five benchmark problems, suggesting that the choice $\beta_2 = 3$ yields the optimal computational efficiency over this class of operators.

4 Benchmark Simulations

We present an overview of the Benchmark simulations for local truncation error $\sigma_{\text{tol}} = 10^{-5}$, for which the PSD scheme is accurate while the IMEX and SAV schemes are borderline accurate. Generically we find that a global $L^2(\Omega)$ discretization error of 3×10^{-2} is generically sufficient to ensure that that scheme is quantitatively accurate, with the correct numbers, types, and placements of defects.

Table 4: L^2 Error between PSD and IMEX or SAV simulations for each benchmark at final time.

Benchmark	PSD/IMEX	PSD/SAV	T
Sub-Critical	8.80E-02	1.46E-01	250
Critical	2.64E-02	3.81E-02	250
Super-Critical	7.18E-01	7.27E-01	250
Foot 1	2.83E-02	6.00E-02	50
Foot 2	3.98E-03	9.90E-03	50

4.1 Sub-critical Benchmark

The sub-critical benchmark has a low level of dispersed diblock polymer material, controlled by the parameter d in (2.15), while the relatively mild concavity of W_q at $u = b_-$, controlled by $\alpha_m(0) = W_q''(b_-)|_{q=0}$, leads to a gentle absorption rate. The bilayer interface profile does not

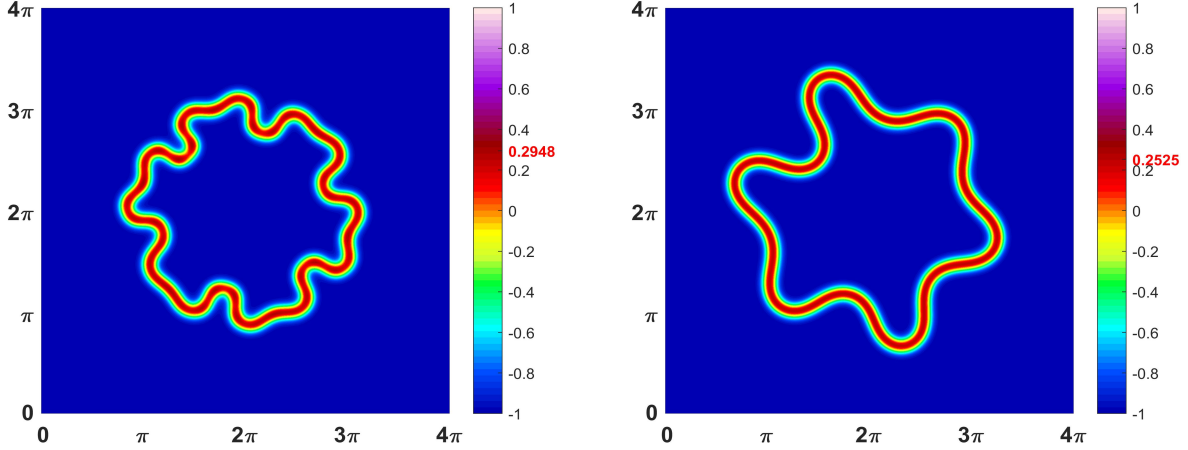


Figure 5: Simulation of sub-critical benchmark 1 with $q = 0$, $\sigma_{\text{tol}} = 10^{-5}$ and $N = 256$ at times $T = 10$ (left) and $T = 250$ (right). All three schemes agree to within L^2 error 1.5×10^{-1} as reported in Table 4. Red number on colorbar indicates $\max u$.

pearl and remains a simple closed curve from initial data to its final equilibrium shape. As shown in [5], gentle absorption drives motion against curvature, regularized by surface diffusion, which relaxes to a curvature driven flow as the background material is depleted. All three schemes are in quantitative agreement, as can be verified by the contour plot comparison in Figure 8 (left) and the data of Table 4.

4.2 Critical Benchmark

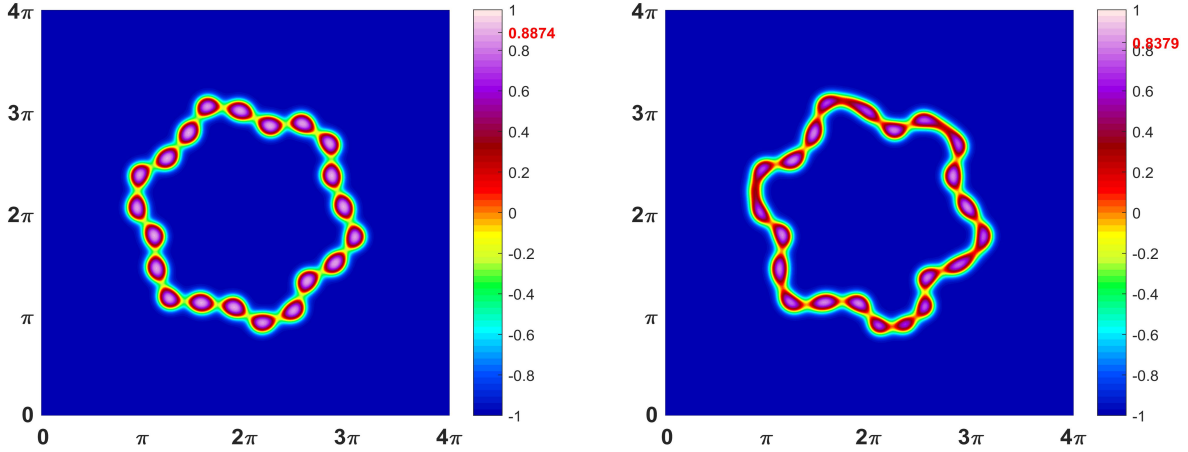


Figure 6: Simulation of the critical benchmark with $q = 0$, $\sigma_{\text{tol}} = 10^{-5}$ and $N = 256$ at times $T = 15$ (left) and $T = 21$ (right). All three schemes agree to within L^2 error 3.9×10^{-2} as reported in Table 4. Red number on colorbar indicates $\max u$.

For the critical case the value of η_2 and d are tuned to create a strongly pearled interface and a long pearled transient, lasting roughly from $T = 4$ to $T = 21$. The bilayer interface pearls transiently, forming 21 pearls, whose discrete count generates a thresholding effect that slows the

absorption of the dispersed amphiphilic polymer as the interface must generate new pearls to lengthen. During the 21-pearl transient period the pearled bilayer interface undergoes a “bicycle chain” meander in which adjacent pearls move in opposite directions, either in towards the center or out towards the boundary of the domain, as can be seen in Figure 6 (left). At time $T = 21$ the pearls have reduced in size, and two extra pearls form at the points of highest curvature. The formation of the additional pearls facilitates an absorption of mass. As the background level of amphiphilic material is depleted the rate of absorption slows and the the interface returns to an unpearled state, similar to that depicted in Figure 5 (right) that is able to move freely in a curvature driven motion. No endcap defects are formed in the critical benchmark, and each of the computational schemes are in quantitative agreement.

4.3 Super-critical Benchmark

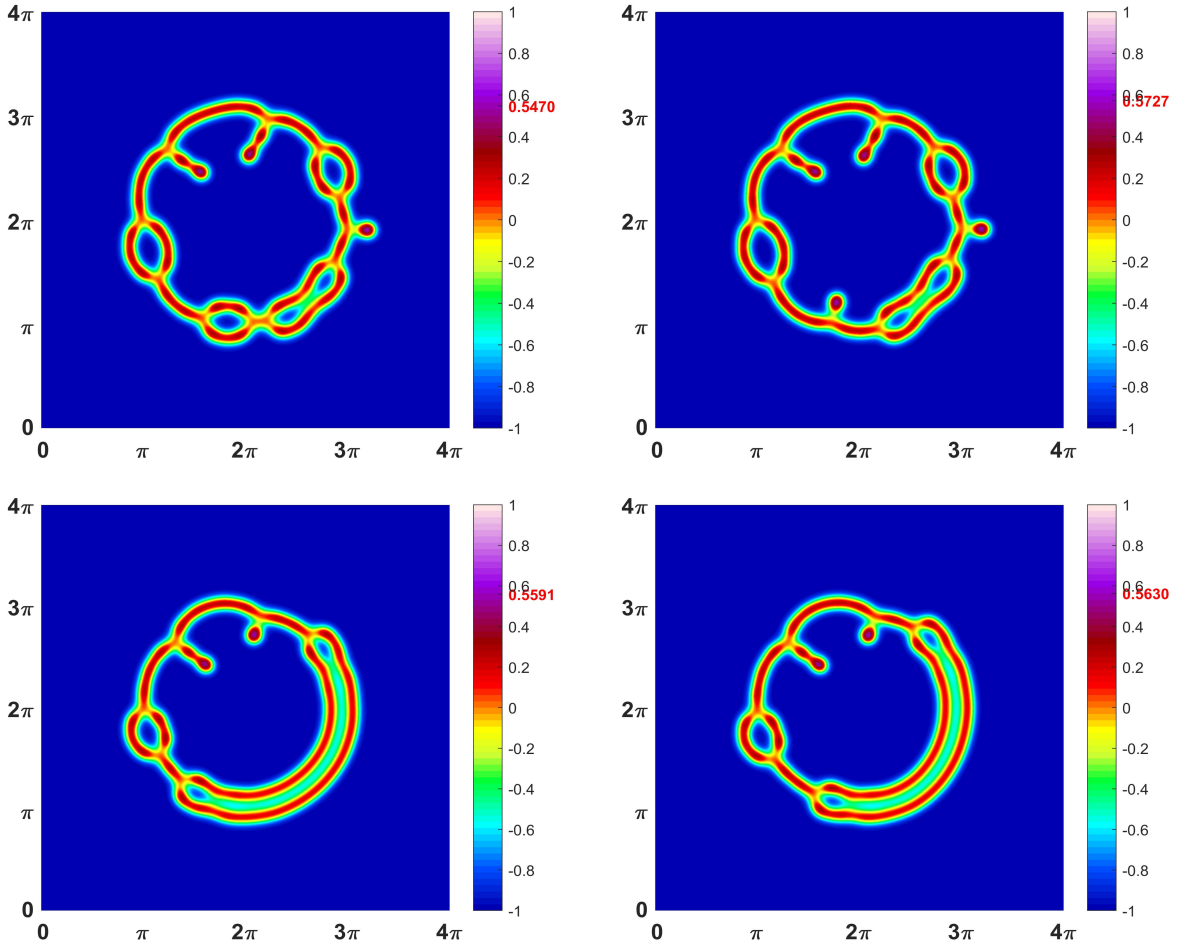


Figure 7: (Top) Simulation of the $q = 0$ super-critical benchmark with $\sigma_{\text{tol}} = 10^{-5}$ and $N = 256$ at time $T = 50$. The top row presents the PSD simulation (left) and the SAV simulation (right). (Bottom) The PSD (left) and SAV (right) simulations at $T = 250$. The IMEX and SAV simulations are very similar, and but both disagree with the PSD simulation by an $O(1)$ in the L^2 norm, as reported in Table 4. Red number on colorbar indicates $\max u$.

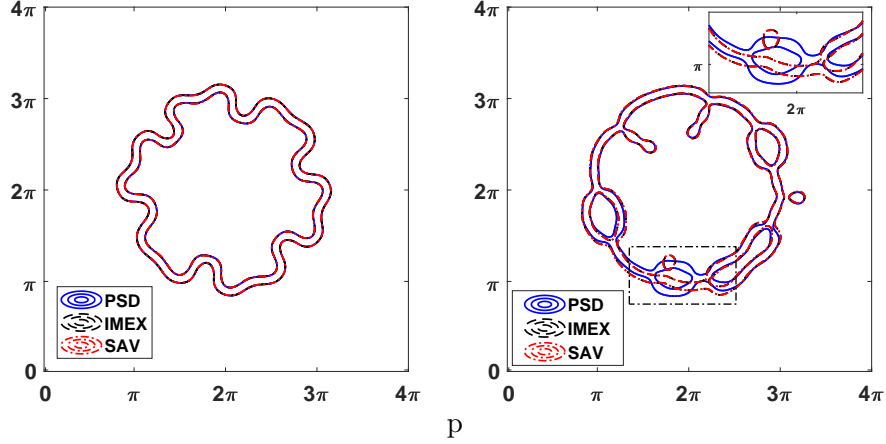


Figure 8: Contour curves from each of the simulations of each of the three schemes with $\sigma_{\text{tol}} = 10^{-5}$ and $N = 256$. The level set $u = -0.12$ for (left) the sub-critical simulation at $T = 10$ and (right) the super-critical benchmark at $T = 50$.

The sub-critical and super-critical benchmarks differ only in the level of the background material, controlled by the parameter d in (2.15). The elevated value of this parameter in the super-critical benchmark increases the rate of arrival of mass to the interface, exceeding the interface's capacity to absorb the arriving mass via a curve lengthening flow or by pearl generation. The interface undergoes defect generation. For the super-critical benchmark with $\sigma_{\text{tol}} = 10^{-5}$ the output from the three schemes disagree at leading order. For the PSD scheme the bilayer interface absorbs material from the background and pearls locally at points of high curvature, and then ejects 8 endcap defects, five of which intersect back with the underlying interface, forming closed loops. Two of the loops subsequently merge to form an extended loop which grows into a cisternal structure characterized by two long parallel interfaces. The IMEX and SAV simulations differ from the PSD, but agree with each other. They also produce 8 endcap defects initially, however only four of them subsequently form closed loops. Two of these loops merge, forming a cisternal structure, however there are two small endcaps in the IMEX and SAV simulations, in contrast to the one small endcap in the PSD simulation. At longer times the cisternal region grows, consuming structures and at time $T = 250$ it leaves one loop, one long endcap, and one short endcap in all simulations – however in the SAV and IMEX simulations the distance between cisternal region and small loop is significantly longer than in PSD simulation. Figure 8 shows the levels sets corresponding to $u = -0.12$ for the sub-critical and super-critical benchmarks with $\sigma_{\text{tol}} = 10^{-5}$ and $N = 256$, showing their agreement in the sub-critical benchmark and their disparity in the super-critical benchmark. In the super-critical benchmark the higher rate of absorption driven by the higher initial background level of u produces dynamic choices associated to endcap formation that require greater accuracy than the linearly implicit schemes can achieve at $\sigma_{\text{tol}} = 10^{-5}$. If σ_{tol} is reduced to 10^{-6} , then PSD simulations does not change quantitatively, while the SAV and IMEX simulations move into

quantitative agreement with the PSD scheme.

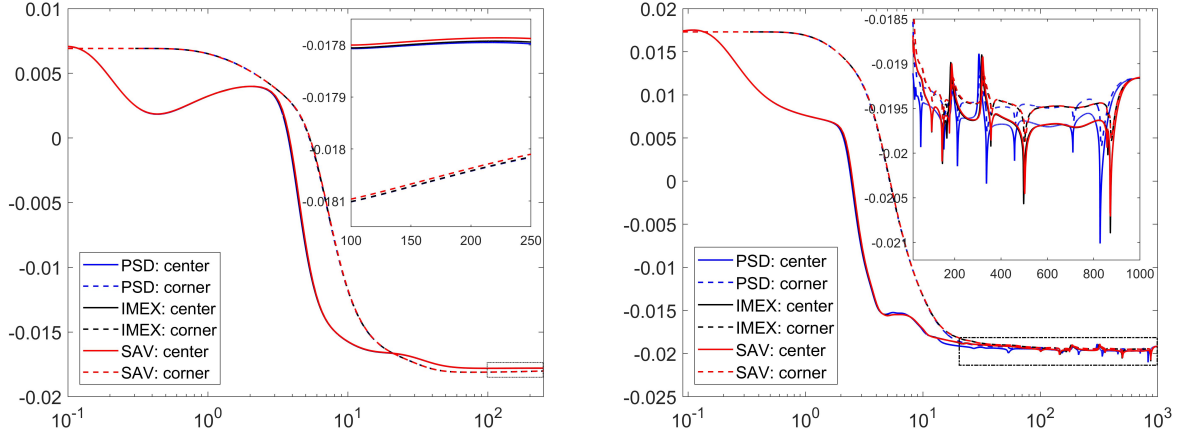


Figure 9: Value of $u - b_-$ at center point (solid) and corner point (dashed) of computational domain for the sub-critical (left) and super-critical (right) benchmarks with $\sigma_{\text{tol}} = 10^{-5}$. Horizontal axis is log of time.

The value of u in the far field, away from the interfacial structure, is asymptotically constant at equilibrium and has been shown to be a key bifurcation parameter for the onset of pearling, [24, 25]. Faithful resolution of this value is essential to an accurate simulation. Figure 9 traces the evolution of the value of $u - b_-$ at the domain center (solid lines) and domain corner (dashed lines) for the three simulation strategies. For the sub-critical simulation no defects are formed and the far-field values of u relax to a tight range of equilibrium values over the time frame $T = 75 \sim 100$. The super-critical simulations have various defect merging events and each is associated with a small excursion in the background levels. In the inset of Figure 9 (right) these excursions can be seen at $T = 200, 350, 450, 725$, and 825 for the PSD scheme. Conversely the linear implicit IMEX and SAV schemes the background levels are in close agreement, recording excursions $T = 175, 360, 500$, and 875 , which differ in both timing and in number of events from the more accurate PSD simulation.

4.4 Foot 1 Benchmark

The Foot 1 and sub-critical benchmarks, are identical in initial data and parameters with the exception of the value of the concavity of the well W_q , controlled by the parameter q . For Foot 1 we take $q = 0.2$ which increases the value of $\alpha_m(q) = W_q''(b_-)$, as depicted in Figure 2. This adjustment raises the energy associated to small, spatially uniform values of u , thereby increasing the rate of absorption of material from the bulk. Although the total amount of material in the background is the same in both benchmarks, the increased absorption rate in the Foot 1 benchmark leads to defect formation. This result is captured by all three schemes with quantitative accuracy, as shown in Table 4. In Figure 10 (left) the pearling and defect formation are visible in the lower-right of the bilayer interface already at time $T = 1.5$. At time $T = 50$ the simulations produce six closed loops placed roughly symmetrically around the bilayer interface. This structure is quasi-stable, but

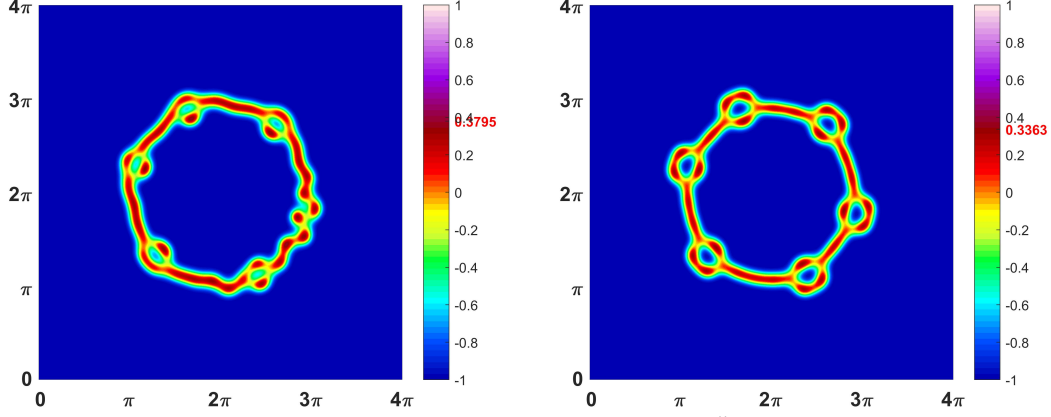


Figure 10: Simulation of Foot 1 benchmark with $q = 0.2$, $\sigma_{\text{tol}} = 10^{-5}$ and $N = 256$ at times $T = 1.5$ (left) and $T = 50$ (right). All three schemes agree to within L^2 error 6×10^{-2} as reported in Table 4. Red number on colorbar indicates $\max u$.

eventually evolves onto a double-sheeted bubble similar to that depicted in the right-most panel of the top row of Figure 18.

4.5 Foot 2 Benchmark

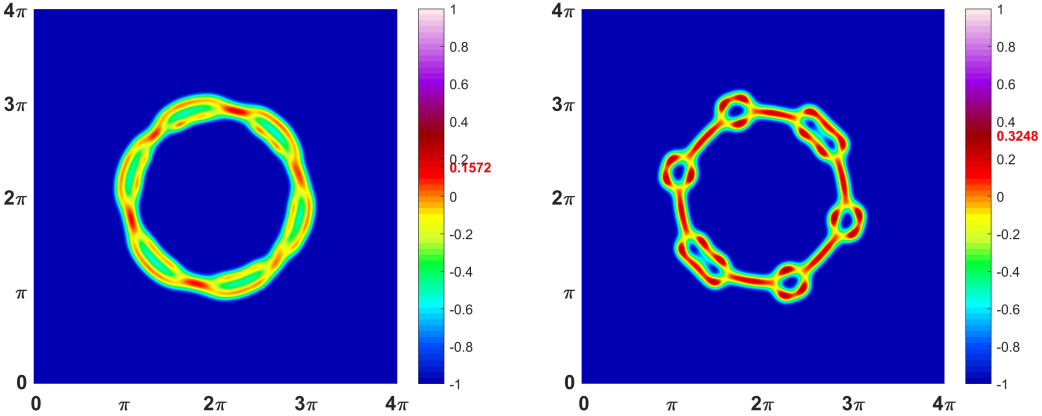


Figure 11: Simulation of the Foot 2 benchmark with $q = 0.2$, $\sigma_{\text{tol}} = 10^{-5}$ at times $T = 1$ (left) and $T = 50$ (right) for $N = 512$. All three schemes agree to within L^2 error 1×10^{-2} as reported in Table 4. Red number on colorbar indicates $\max u$.

The Foot 2 and sub-critical benchmarks have an identical setup with the exception of the value of q , which is taken as $q = 0.5$ in Foot 2. This introduces a very strong nonlinear stiffness, and the large value of $\alpha_m = W_q''(b_-)|_{q=0.5}$ significantly increases the energy penalty associated to dispersed amphiphilic material. As a consequence its rate of absorption onto the bilayer interface increases, inducing a curve-splitting bifurcation in which the bilayer interface splits directly in two, as shown in Figure 11 (left) at $T = 1$. All three schemes agree qualitatively on the 512×512 mesh, producing four loops and two double loop. Grid refinement showed that the $N = 256$ grid was insufficient to produce accurate results. Further grid refinement to $N = 1024$ yields quantitative agreement with

the $N = 512$ simulations. The large value of $W_q''(b_-)$ for $q = 0.5$ yields a profile that is much less smooth. The spatial convergence to the far-field value occurs at the exponential rate $\sqrt{W_q''(b_-)}/\varepsilon$, which is significantly greater for $q = 0.5$, necessitating the higher spatial resolution.

Table 5: L^2 Grid Refinement Error.

N	256 / 512	512 / 1024
Sub-Critical	6.218E-04	
Super-Critical	2.589e-04	
Critical	3.827E-04	
Foot 1	8.502E-02	
Foot 2	1.008	5.762E-04

Table 6: L^2 Temporal Convergence Error and Rates. The error is determined by comparison to PSD with a fixed temporal step size $k = 10^{-6}$ and $i_{\text{tol}} = 10^{-11}$.

	IMEX		PSD		SAV	
fixed k	L^2 Error	Rate	L^2 Error	Rate	L^2 Error	Rate
$2^3 \times 10^{-2}$	2.20E-01		7.03E-05			
$2^2 \times 10^{-2}$	5.38E-02	2.03	1.77E-05	1.99		
$2^1 \times 10^{-2}$	1.37E-02	1.98	4.43E-06	2.00	2.50E-02	
$2^0 \times 10^{-2}$	3.54E-03	1.95	1.11E-06	2.00	6.46E-03	1.95
$2^{-1} \times 10^{-2}$	9.31E-04	1.93	2.79E-07	1.99	1.70E-03	1.93
$2^{-2} \times 10^{-2}$	2.46E-04	1.92	8.36E-08	1.74	4.52E-04	1.91
$2^{-3} \times 10^{-2}$	6.47E-05	1.93	6.89E-08	0.28	1.20E-04	1.91
$2^{-4} \times 10^{-2}$	1.69E-05	1.94	6.62E-08	0.06	3.17E-05	1.92
$2^{-5} \times 10^{-2}$	4.37E-06	1.95	5.81E-08	0.19	8.24E-06	1.94
$2^{-6} \times 10^{-2}$	1.12E-06	1.96	7.58E-08	-0.38	2.12E-06	1.96

The time-trace of the background levels, $u - b_-$ evaluated at the domain center (solid) and domain corner (dashed), are presented for the Foot 2 benchmark in Figure 12 (left). It has several notable differences from the sub-critical benchmark presented in Figure 9 (left). The most salient distinction is that the large value of $\alpha_m(0.5)$ greatly increases the temporal rate of absorption of amphiphilic material from the background. For the Foot 2 benchmark the background state begins to achieve its equilibrium value at $T = 1$ and is fully equilibrated around $T = 7 \sim 8$. This is roughly 10-15 times faster than the relaxation for the $q = 0$ sub-critical benchmark, depicted in Figure 9. The only difference in the two benchmarks is the increase in concavity of the well W_q near $u = b_-$, reflected in Figure 2(bottom-right).

5 Computational Accuracy and Efficiency

The three schemes presented here are 2nd order accurate, as verified by the convergence study presented in Table 6. Nevertheless, the performance of the schemes is not equally accurate nor efficient, particularly as the nonlinear stiffness parameter q is increased. We discuss the relation of accuracy to energy decay, global discretization error, and computational efficiency.

5.1 Energy Decay

A major feature of gradient schemes is the decay of the overall system energy. Much attention has been given to the construction of gradient stable schemes for which energy decay is unconditional with respect to the temporal step-size. However in gradient flows that generate a rich variety of structures issues of accuracy move to the forefront and energy decay ideally becomes a consequence of accuracy. For the super-critical benchmark, the various competing outcomes have only marginally different energies and considerable accuracy is required for a scheme to differentiate between the available options. As shown in Figure 13 (left), with $\sigma_{\text{tol}} = 10^{-5}$ for each of the 5 benchmarks the energy decay behavior is very similar and decays uniformly. There are however important differences. As the middle inset shows, for the super-critical benchmark the energy trace for the IMEX and SAV simulations are almost indistinguishable, while the PSD simulation shows visible deviations in system energy, at roughly a 1% relative error. In these simulations the PSD scheme is more accurate and the linear-implicit schemes produce output that is erroneous to leading order in the L^2 norm. The differences in energy decay, and solution u , are largely erased for IMEX and SAV when σ_{tol} is reduced to 10^{-6} . The second inset shows detail of the Foot 1 benchmark. In this case the PSD and IMEX schemes have quantitative agreement, while the SAV scheme produces a simulation whose energy proceeds downhill too quickly at $T = 650$. This leads to an output that is time-shifted forward by about 200 units. Again, these errors in energy decay are eliminated by reducing σ_{tol} to 10^{-6} . These features emphasize that system energy can be a poor proxy for accuracy, and that energy decay is generally a minor benchmark for a gradient flow.

The time-stepping profiles for the IMEX and SAV schemes are remarkably similar, and differ in important ways from that of the PSD scheme. As shown in Figure 12 (right), the PSD generically takes the largest time step-sizes, and typically hits the maximum step-size ceiling k_{max} shortly after the resolution of the initial transient. This ceiling is required to insure the convergence of the nonlinear iterative scheme and to optimize its performance as measured by FFT per time unit. This value is smaller for the stiffer Foot 2 benchmark than for the super-critical benchmark. Indeed the time-step profile for PSD is largely equivalent for the super-critical and the Foot 2 benchmarks, until it hits the lower value of k_{max} for the Foot 2 benchmark. This is in contrast to the IMEX and SAV profiles which are different for the two benchmark problems, but largely agree with each

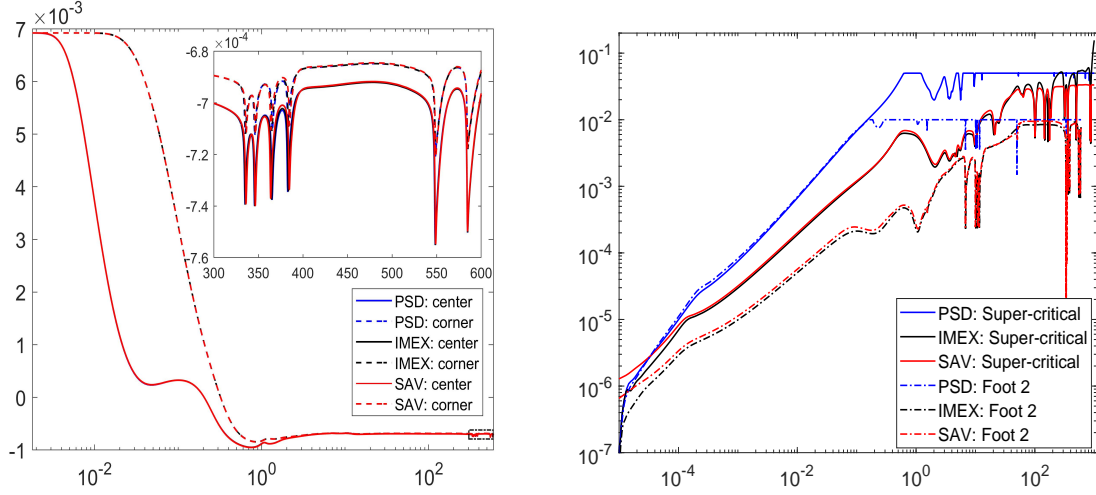


Figure 12: (left) Value of $u - b_-$ at center point (solid) and corner point (dashed) of the computational domain for the $q = 0.5$ Foot 2 benchmark for $\sigma_{\text{tol}} = 10^{-5}$ and $N = 512$. (right) Evolution of the adaptive temporal step-size on a log-log scale for each of the three schemes for the super-critical benchmark (solid) and the $q = 0.5$ Foot 2 benchmark (dashed). Horizontal axis is log of time.

other. Each of the schemes has swings in step size of roughly one order of magnitude during the various defect generation and merging events that occur after the initial transient. The step sizes for the IMEX and SAV schemes are generically smaller than those for PSD, by as much as two orders of magnitude for the stiffer Foot 2 benchmark. However this is offset by the growing number of iterations required for solving the stiffer nonlinear system in this problem.

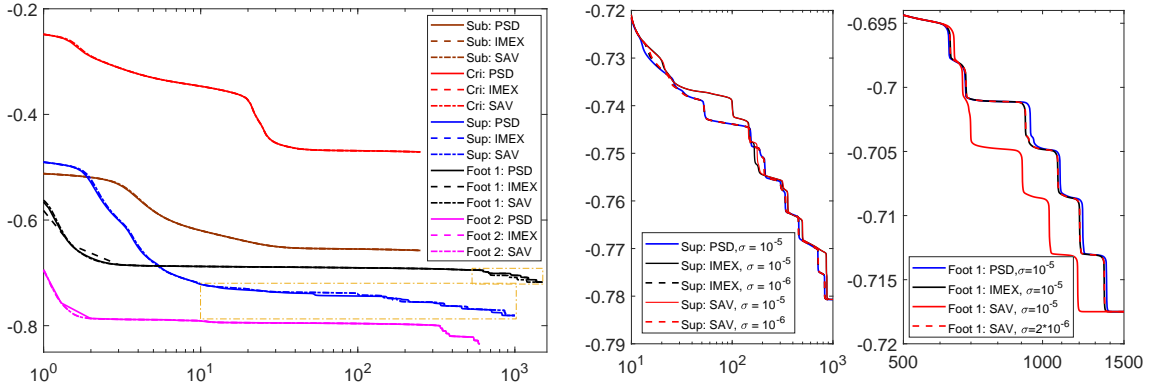


Figure 13: (left) System energy versus time on a semilog-x scale for each of the five benchmark problems for each scheme with $\sigma_{\text{tol}} = 10^{-5}$ on a semilog-x scale. The boxed insets for the super-critical (middle) and foot 1 (right) benchmarks show more detail and include results for IMEX and SAV with $\sigma_{\text{tol}} = 10^{-6}$.

An excellent proxy for accuracy is to determine the lowest (critical) value of the background level, as measured by the initial data parameter d in (2.15), at which the a defect is generated within the flow. The onset of a defect is easily detected through the maximum value of u , as the maximum value of the bilayer profile is determined by the largest zero of W_q , for (2.13) about $u = 0.3566$, while defects and higher codimensional structures such as micelles reside much more

deeply in the right well of W_q , with maximum values close to $u = 0.74$. Tracking the temporal evolution of $\max u$ yields a strong dichotomy. We fixed the parameters as in the critical benchmark problem but slightly adjusted the value of d to modify the amount of amphiphilic material in the bulk. The critical d value, reported in Table 7 depends upon the local truncation error, but converges to a common value of $d = 0.7526$ with decreasing σ_{tol} . Indeed the correct critical value is achieved by the PSD scheme at $\sigma_{\text{tol}} = 10^{-7}$ but requires reduction of σ_{tol} to 10^{-8} for IMEX and SAV. The time evolution of $\max(u(\cdot, t))$ for the critical benchmark parameters but seven different value of d is presented in Figure 14.

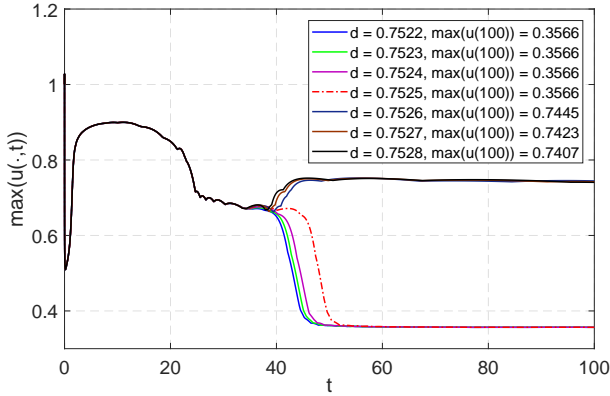


Figure 14: Running value of $\max u$ from the PSD scheme for the critical benchmark problem with $d = 0.7522, \dots, 0.7728$ in increments of 0.0001 when $\sigma_{\text{tol}} = 10^{-7}$. The onset of a defect occurs at the critical value $d = 0.7526$.

Table 7: The dependence of the critical value of d in (2.15) upon σ_{tol} for each scheme.

σ_{tol}	PSD	IMEX	SAV
10^{-5}	0.7527	0.7540	0.7554
10^{-6}	0.7525	0.7529	0.7532
10^{-7}	0.7526	0.7527	0.7527
10^{-8}	0.7526	0.7526	0.7526

5.2 Global Discretization Error versus Computational Cost

The definitive measure of accuracy is to compute the global discretization error of a simulation as measured against a known highly accurate answer. To produce these highly-accurate solutions we conducted a spatial grid refinement study for each benchmark problem and each computational scheme. For all but the stiffest Foot 2 benchmark increasing the grid from $N = 256$ to $N = 512$ produced consistent results, with solution differences reported in Table 5. We present results only to the accuracy determined within this grid refinement study. Specifically the highly accurate simulations were calculated with the PSD scheme with $\sigma_{\text{tol}} = 10^{-9}$ for $q = 0$, and with $\sigma_{\text{tol}} = 3 \times 10^{-8}$ for $q = 0.2$. For $q = 0.5$, the IMEX scheme with $\sigma_{\text{tol}} = 3 \times 10^{-9}$ was used. The output of these simulations are taken as the highly accurate simulation against which others are compared. For all three schemes, sufficient refinement of σ_{tol} lead to a global error that was within the anticipated accuracy of the scheme. Indeed our computations find that a global $L^2(\Omega)$ discretization error of 3×10^{-2} is generically sufficient to ensure that that scheme is quantitatively accurate, with the correct numbers, types, and placements of defects.

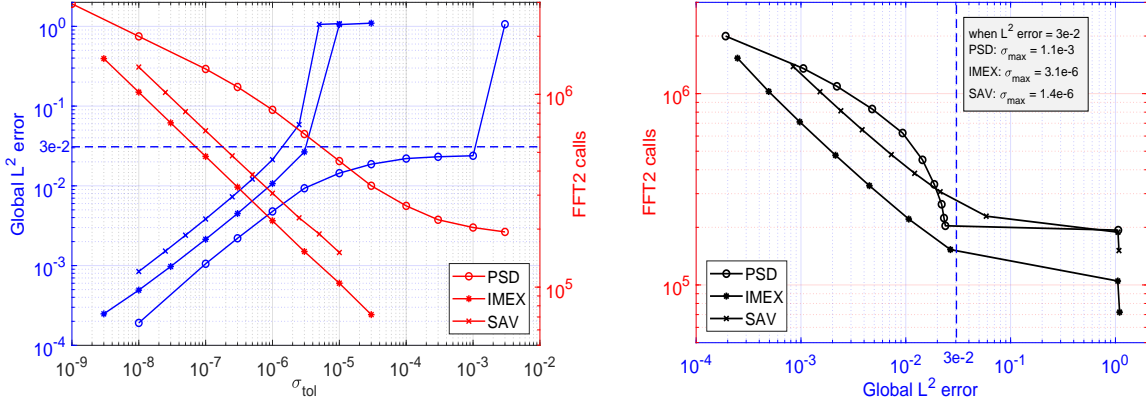


Figure 15: (left: blue y-axis and lines) Global L^2 error versus σ_{tol} at $T = 250$ for the super-critical benchmark as measured by comparison to the most accurate solution. (left: red y-axis and lines) Computational cost versus σ_{tol} as measured by total number of FFT calls. (right) Computational cost versus global L^2 error, plotted parametrically in σ_{tol} .

We measure the computational efficiency of the three schemes in two ways. First as global discretization error, G_{tr} , versus σ_{tol} , and then more meaningfully as global discretization error versus FTT calls. This latter is euphemistically referred to as the dollars-per-digit metric. The first result, presented in Figure 15 (left), shows the decay in global L^2 error with decreasing σ_{tol} . The blue curves, corresponding to the left (blue) vertical axis, show that IMEX, PSD, and SAV all improve in global accuracy with decreasing σ_{tol} . For the super-critical benchmark the linear-implicit IMEX and SAV schemes are inaccurate for $\sigma_{\text{tol}} > 4 \times 10^{-6}$ and then have global discretization errors that decay linearly on a log-log plot, corresponding to a global discretization error roughly proportional to the $2/3$ power of the local truncation error. Conversely, the PSD is accurate for all $\sigma_{\text{tol}} < 1 \times 10^{-3}$, but its global accuracy at first improves sub-linearly with σ_{tol} on the log-log scale before setting into the $2/3$ power law relation between global discretization and local truncation errors. For the linear-implicit schemes the workload as measured by total FFT calls is remarkably linear as function of local truncation error on the log-log curve. Their workload grows approximately as a $-1/3$ power of the local truncation error over three orders of magnitude, with the IMEX more efficient than the SAV by a fixed factor of 2 over this range. The PSD workload starts out significantly higher than the linear-implicit schemes, but grows more slowly. To make a more meaningful comparison of the data it is instructive to plot the FTT calls versus the global discretization error, with σ_{tol} acting as a parameterization of the curve. This is shown in Figure 15 (right). In this plot, the lowest curve attains the desired global discretization error with the least computation cost.

Setting $G_{\text{tr}} = 3 \times 10^{-2}$ as an acceptable upper limit, we find that the three schemes achieve this global tolerance at comparable computational costs that correspond to disparate local truncation errors. The IMEX scheme is the most efficient, hitting the global accuracy mark with 1.5×10^5 FFT

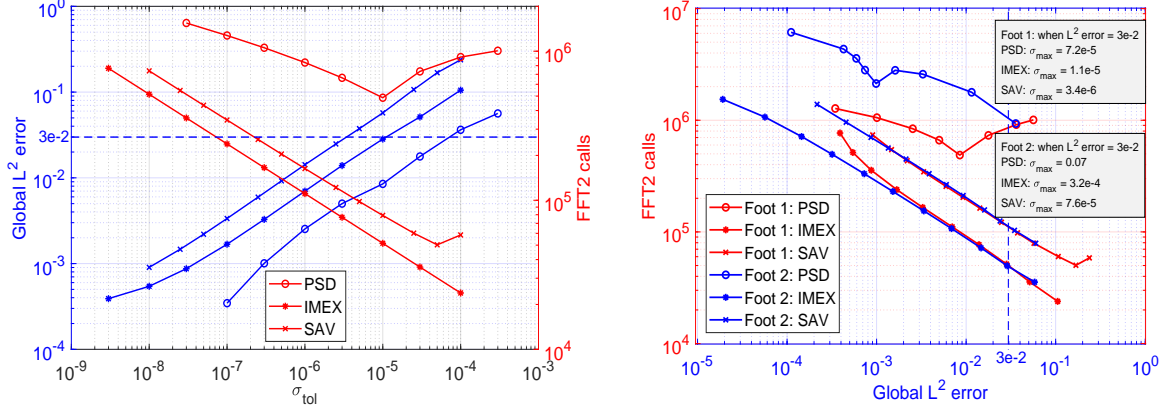


Figure 16: (left: blue y-axis and lines) Global L^2 error versus σ_{tol} at $T = 50$ for the $q = 0.2$ Foot 1 benchmark as measured by comparison to the most accurate solution. (left: red y-axis and lines) Computational costs versus σ_{tol} as measured by total number of FFT calls.

calls at $\sigma_{\text{tol}} = 3 \times 10^{-6}$, while PSD does so with 2×10^5 FFT calls at a much lower $\sigma_{\text{tol}} = 10^{-3}$, and SAV at 2.5×10^5 FFT calls and $\sigma_{\text{tol}} = 10^{-6}$. However the efficiency of the PSD code decays relatively rapidly with global error above this acceptable upper limit, recovering at very small global error. The overall result is a large interval in which the linear-implicit schemes outperform PSD. For the stiffer Foot 1 benchmark simulations with $q = 0.2$ the linear-implicit schemes perform at a similar level to the $q = 0$ benchmarks, while the nonlinearly implicit PSD struggles due to convergence issues in its nonlinear solver. As shown in Figure 16 (left), the global error for each scheme is an approximately linear function of local truncation error on the log-log scale, corresponding to a power law exponent in the range $0.5 \sim 0.6$ that is slightly reduced from the $2/3$ exponent observed for the super-critical benchmark. The computational efficiency plot, Figure 16 (right), the data for both the Foot 1 and Foot 2 benchmarks are compared. The linear-implicit schemes substantially outperform the nonlinear-implicit PSD, with the IMEX remaining roughly twice as efficient as SAV over two orders of magnitude of global discretization error. For the linear-implicit schemes the computational cost is very similar for Foot 1 and 2, with the Foot 2 simulations slightly more accurate due to the increase in spatial resolution to $N = 512$. Conversely, the nonlinear-implicit PSD requires significantly more effort with increasing q as the iteration count in the nonlinear solver increases significantly. The minimal cost for SAV to achieve the acceptable global discretization error is roughly twice that of IMEX, while for Foot 1 PSD is most efficient at a lower global error of 9×10^{-4} , for which it requires 10 times the effort of IMEX and for Foot 2 PSD requires 40 times the computational effort of IMEX. It is worth noting that PSD is more comparatively more efficient at lower global error; indeed it requires only 3 and 7 times the computational effort of IMEX to achieve an error of 9×10^{-4} for the Foot 1 and Foot 2 benchmarks, respectively.

In Figure 17 the temporal trace of the global error is plotted for local truncation errors of $\sigma_{\text{tol}} = 10^{-5}, 10^{-6}$, and 10^{-7} . In all cases the PSD is the most accurate, generically by an order

of magnitude at the same local truncation error. However the accuracy for PSD increases only modestly with decreasing σ_{tol} while SAV and IMEX schemes have more significant improvements. For the sub-critical benchmark the global error accumulates slowly in each of the schemes as the shape of the interface evolves and inaccuracies in its location accumulate. For the super-critical benchmark the error has peaks at each of the major defect merging events that occur at $t = 50, 150, 185, 210$. These peaks reflect the impact of slight timing errors in the defect merging events and in the spatial structure of the merging transient. Each scheme shows about a half-order of magnitude loss of accuracy during the merging that is recovered afterwards. This holds except for the SAV and IMEX schemes with $\sigma_{\text{tol}} = 10^{-5}$ which are both insufficiently accurate to capture the correct sequencing of the defect evolution.

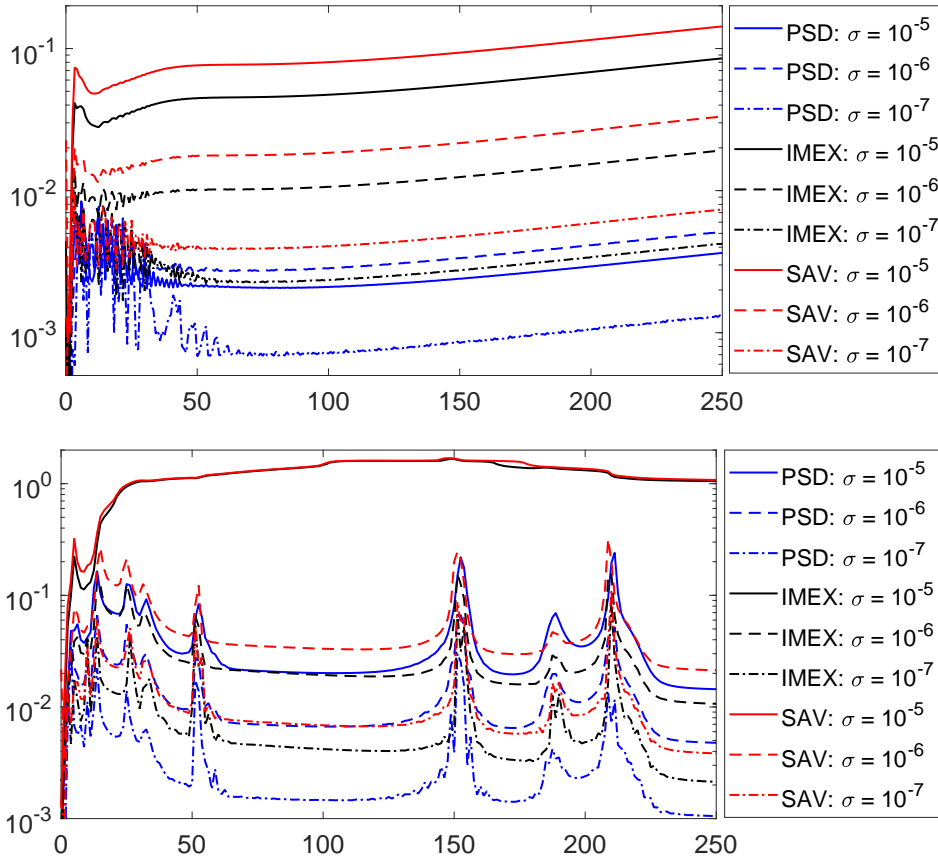


Figure 17: Time evolution of the global L^2 error between output of the three schemes and the highly accurate solution for $\sigma_{\text{tol}} = 10^{-5}, 10^{-6}$, and 10^{-7} for (top) the sub-critical benchmark and (bottom) the super-critical benchmark.

6 Conclusion

We have demonstrated that the morphological complexity that develops within the gradient flows of the FCH energy requires accuracy for faithful representation. More significant than energy decay is

energy accuracy, indeed small errors in evaluation of energy of different configurations can generate alternate temporal evolutions resulting in errors that grow to become leading order. The impact of this is magnified as the nonlinear stiffness in the model is increased. The nonlinear solve required in the more strongly implicit PSD approach tends to raise the overall accuracy of the scheme, and for less-stiff forms of the model this compensates for the increased computational effort required for the iterative solver. The result is that the linear-implicit and nonlinear-implicit models are comparable. However for the more nonlinearly stiff versions of the model, the linear-implicit schemes require no tuning and experience only modest decline in efficiency, while the nonlinear-implicit PSD requires tuning of the error tolerance and maximum time-step parameters to optimize its performance. Despite this tuning the efficiency of the PSD scheme falls behind the linear-implicit schemes by a factor that is comparable to the increase in stiffness, as measured by the left-well concavity $\alpha_m(q) = W_q''(b_-)$.

Within the linear-implicit schemes the performance of the IMEX and the SAV schemes are almost indistinguishable. Their global accuracy as a function of local truncation error are almost identical. The only discrepancy lies in the computational effort which is routinely a factor of two larger for the SAV scheme. This is likely a result of the extra steps required to resolve the larger SAV system of equations. Beyond the guarantee of the decay of the associated pseudo-energy, it is difficult to identify a feature in the SAV scheme in which it improves upon the simpler IMEX approach. Far and away the most important feature of the linear-implicit schemes is selecting a proper linear term for the implicit step. Given the theoretical understanding of the importance of the background state, that is of the value of u away from non-trivial structures, it is reasonable and efficient to use the linearization about the spatially constant state $u \equiv b_-$. We generalized this to the family of operators presented in (3.15), and found that a choice of $\beta_1 + \beta_2 \approx 3$ provided optimal performance. The choice $\beta_1 = 2$ and $\beta_2 = 1$ corresponds to the linearization about the spatially constant background state. These constant coefficient linear operators are trivially inverted in the spatially periodic setting considered herein. It certainly may not be the case that such a convenient and efficient linear-implicit operator is available in all systems.

As a final demonstration of the complexity possible within the FCH gradient flow, we present a series of computations that show a putative equilibrium state resulting from the gradient flow of the initial data from the super-critical benchmark, see Figure 18. The only variation is in the value of the parameter η_2 , which represents the aspect ratio of the amphiphilic molecule. The decreasing values of η_2 correspond to the increasing values of w_{PEO} in the horizontal axis of the experimental bifurcation diagram presented in Figure 1. Perhaps the fundamental contribution of this numerical study the suggestions that the shapes of the final structures produced in these casting problems are not uniquely determined by the properties and densities of the molecules they are composed of, but also depend upon the history of the morphology. Once defects are induced by transient flow, they

become an integral part of the energy landscape and can snag the gradient flow at a rich variety of local minima. These gradient flow transients form an intriguing phylogenesis, whose resolution requires significant accuracy.

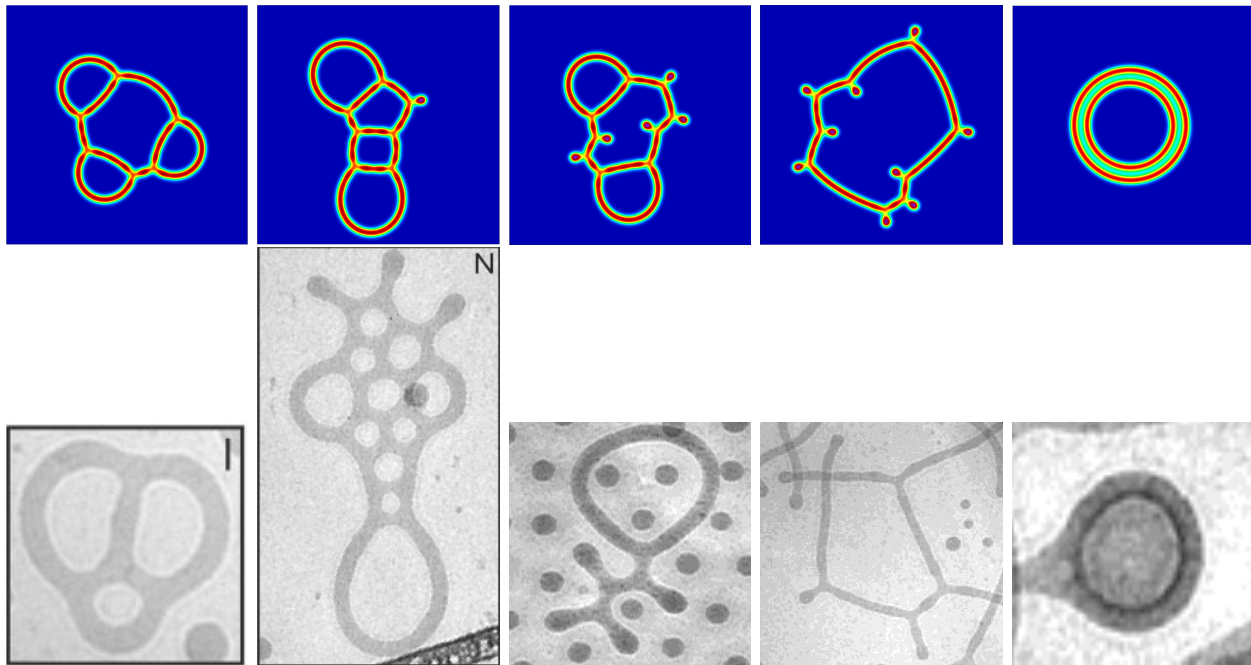


Figure 18: (top-row) Approximate equilibrium states computed from super-critical benchmark initial data and parameters except for values of η_2 taken as $2.55\epsilon, 2.6\epsilon, 2.65\epsilon, 2.8\epsilon, 2.85\epsilon$ (left-to-right). Final times are $T = 5K, 50K, 100K, 50K, 3K$ respectively. (bottom-row) Experimental comparisons showing (left-to-right) bubbles, bubbles with endcaps, bubbles and branched endcaps, long-branched filaments with endcaps, and double-sheeted bubbles (bubble inside of bubble). Figures 3I and 3N from [22], reprinted with Permission from the AAAS. Figures 5A, 5B, and 9C, Reprinted (adapted) with permission from [23]. Copyright (2004) American Chemical Society.

Acknowledgement

A. Christlieb acknowledges support from NSF grant DMS-1912183. K. Promislow acknowledges support from NSF grant DMS-1813203. Z. Tan recognizes support from the China Scholarship Council under 201906160032. B. Wetton recognizes support from a Canadian NSERC grant. S. Wise recognizes support from NSF grant DMS-1719854.

References

- [1] S. Barnhill, N. Bell, J. Patterson, D. Olds, and N. Gianneschi, Phase diagrams of polynorbornene amphiphilic block copolymers in solution, *Macromolecules* **48** (2015) 1152-1161.
- [2] A. Blanazs, S.P. Armes, and A. J. Ryan, Self-assembled block copolymer aggregates: from

- micelles to vesicles and their biological applications, *Macromolecular rapid communications*, **30** (2009) 267–277.
- [3] L. Chen, Xiaozhe Hu, and S.M. Wise, Convergence Analysis of the fast Subspace Descent Method for Convex Optimization Problems, *Math. Comp.* (in press), <https://doi.org/10.1090/mcom/3526>.
 - [4] Y. Chen, A. Doelman, K. Promislow, F. Veerman, *Robust stability of multicomponent membranes: the role of glycolipids*, submitted (2019).
 - [5] Y. Chen and K. Promislow, Regularized curve lengthening in the strong FCH gradient flow. arXiv preprint: <https://arxiv.org/abs/1907.02196>
 - [6] Y. Chen and K. Promislow, Amphiphilic blends, derivation of a density functional theory. Preprint.
 - [7] S.-H. Choi, T. Lodge, and F. Bates, Mechanism of molecular exchange in diblock copolymer micelles: hypersensitivity to core chain length, *Phys. Rev. Lett.* **104** (2010) 047802.
 - [8] R. Choksi and S. Ren, On the derivation of a density functional theory for microphase separation of diblock copolymers, *Journal of Statistical Physics* **113** 151-176 (2003).
 - [9] R. Choksi and X. Ren, Diblock copolymer/homopolymer blends: Derivation of a density functional theory. *Physica D* **203**(1-2) (2005), 100-119.
 - [10] A. Christlieb, N. Kraitzman, K. Promislow, Competition and Complexity in Amphiphilic Polymer Morphology, *Physica D* **400** 132144 (2019).
 - [11] S. Dai and K. Promislow, Geometric Evolution of Bilayers under the Functionalized Cahn-Hilliard equation, *Proc. Roy. Soc. London, Series A*, **469** : 20120505 (20 pages).
 - [12] S. Dai and K. Promislow, Competitive Geometric Evolution of Amphiphilic Interfaces, *SIAM Math. Analysis* **47** (2015), 347-380.
 - [13] Q. Du, L. Ju, X. Li, and Z. Qiao, Stabilized linear semi-implicit schemes for the nonlocal Cahn-Hilliard equation, *J. Computational Physics* **363** (2018) 39-54.
 - [14] W. Feng, Z. Guan, J.S. Lowengrub, X. Wang, S.M. Wise, and Y. Chen, A uniquely solvable, energy stable numerical scheme for the functionalized Cahn–Hilliard Equation and its convergence analysis, *J. Sci. Computing* **76** (2018) 1938-1967.
 - [15] W. Feng, A.J. Salgado, C. Wang, and S.M. Wise, Preconditioned Steepest Descent Methods for some Nonlinear Elliptic Equations Involving p-Laplacian Terms, *J. Comput. Phys.* **334** (2017) 45-67.

- [16] G. Fredrickson, The equilibrium theory of inhomogeneous polymers, International Series of Monographs on Physics 134, Oxford: Clarendon Press, (2006).
- [17] N. Gavish, G. Hayrapetyan, K. Promislow, L. Yang, Curvature driven flow of bi-layer interfaces, *Physica D* **240** (2011) 675-693 .
- [18] G. Gompper and J. Goos, Fluctuating interfaces in microemulsion and sponge phases, *Phys. Rev E*. **50** (1994) 1325-1335.
- [19] G. Gompper and M.Schick, Correlation between structural and interfacial properties of amphiphilic systems, *Phys. Rev. Lett.* **65** (1990) 1116-1119.
- [20] U Gong, J. Zhao, and Q. Wang, Arbitrarily high-order unconditionally energy stable schemes for gradient flow models using the scalar auxiliary variable approach, arXiv preprint arXiv:1907.04254 (2019).
- [21] E. Hairer, G. Wanner, and S. P. Nørsett, Solving ordinary differential equations, I, Nonstiff problems. Springer, Berlin, (1993).
- [22] S. Jain and F.S. Bates, On the origins of morphological complexity in block copolymer surfactants, *Science*, **300** (5618):460–464 (2003).
- [23] S. Jain and F. Bates, Consequences of nonergodicity in aqueous binary peo-pb micellar dispersions. *Macromolecules*, **37** (2004) 1511–1523.
- [24] N. Kraitzman and K. Promislow, Pearling Bifurcations in the strong Functionalized Cahn-Hilliard Free Energy, *SIAM Math Analysis* **50** (3) 3395-3426 (2018), DOI:10.1137/16M1108406
- [25] K. Promislow and Q. Wu, Existence of pearled patterns in the planar Functionalized Cahn-Hilliard equation, *J. Differential Equations* **259** (2015) 3298-3343.
- [26] J. Shen, J. Xu, and J. Yang, The scalar auxiliary variable (BDF2-SAV) approach for gradient flows, *J. Computational Physics* **353** (2018) 407-416
- [27] J. Shen and J. Xu, Convergence and error analysis for the scalar auxiliary variable (BDF2-SAV) schemes to gradient flows, *SIAM Numerical Analysis* **56** (2018) 2895-2912.
- [28] J. Shen, J. Xu, and J. Yang, A New Class of Efficient and Robust Energy Stable Schemes for Gradient Flows, *SIAM Rev.* **61** (3), 474-506.
- [29] M. Teubner and R. Strey, Origin of scattering peaks in microemulsions, *J. Chem. Phys.* **87** (1987) 3195-3200.

- [30] T. Uneyama and M. Doi, Density Functional Theory for Block Copolymer Melts and Blends, *Macromolecules* **38** 196-205.
- [31] T. Uneyama and M. Doi, Calculation of the Micellar Structure of Polymer Surfactant on the Basis of Density Functional Theory, *Macromolecules* **38** 5817-5825.
- [32] B.P. Vollmayr-Lee and A.D. Rutenberg, Fast and accurate coarsening simulation with an unconditionally stable time step *Phys. Rev. E* **68**, 066703 (2003).
- [33] S. Wise, Unconditionally stable finite difference, nonlinear multigrid simulation of the Cahn-Hilliard-Hele-Shaw system of equations, *J. Sci. Computing* **44** (2010) 38-68.
- [34] C. Zhang, J. Ouyang, C. Wang, and S.M. Wise, On Modified-Energy Stable SAV-Type Schemes for the Functionalized Cahn-Hilliard Equation: Benchmarks and Comparisons with Classical BDF Methods, *J. Comput. Phys.* submitted.